

Chapter 1 Introduction

1.1 Need for the Miniature Pressure Sensors

Miniature pressure sensors have long been pursued in industrial, medical and research fields. The advantages of small size and light weight open up numerous opportunities in applications such as medical diagnostics, environmental monitoring and other industrial applications, such as structural health monitoring and damage detection. Such systems must satisfy many requirements, including low cost, robustness and real-time data processing. In many applications, the device must also be disposable after a single usage. ^[1]

1.1.1 Medical Applications

In the medical community, there has been a continuing upward trend in the popularity of minimally invasive techniques. Taking advantage of natural body orifices or small incisions, physicians are able to dramatically reduce patient trauma, decrease procedure time, and accelerate recovery. Optical fiber has been utilized for the direct visualization of the gastrointestinal tract, bronchial system, and vasculature. ^[2]

Invasive pressure measurement, which is of great importance in medical diagnostics, is a good example. Monitoring of arterial or venous blood pressure, coronary, pulmonary and intracranial pressure measurements are only a few examples where accurate, robust and small disposable sensors are needed.

Today most invasive pressure measurements utilize fluid filled catheter that transfers measured pressure to external transducer. As illustrated in Figure 1-1, the system includes an intravascular catheter, a liquid-filled tubing system to transmit pressure waves, and an external pressure transducer to convert the information into an electrical signal.

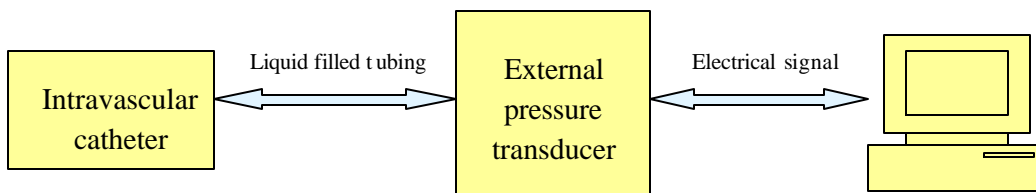


Figure 1-1 Current medical invasive pressure system

Such a system is susceptible to many problems. Its bulky size makes it difficult to apply in small blood vessels or newborns. In addition, fluid inertia, air bubbles in the

tubing, and the elasticity of the tubing can severely limit the time response.

Fiber optic sensor provides an attractive solution for invasive pressure measurements due to the biocompatibility of SiO₂, electrical passivity and EMI immunity. Furthermore, optical fiber is inexpensive and ecologically acceptable, which is important for disposable medical equipment.

1.1.2 Industrial Applications

In the industrial community, miniature pressure sensors that can endure extremely high temperatures, high pressures and corrosive environments are in great demand. For example, pressure testing is commonly required in oil well downholes, jet engines, and power generation equipment, where the space for sensor installation is limited and the environment is harsh. These requirements impose severe constraints on the sensor design and material composition. Also, since temperature can fluctuate in extreme environments, the pressure sensor for these extreme environments will ideally have negligible sensitivity to temperature.^[3]

Most current pressure sensors, which are electrically based, suffer from many inherent problems, such as strong temperature dependence, electromagnetic interference, bulky size, and poor performance in terms of mechanical properties, temperature endurance, accuracy, reliability, long time stability, repeatability, etc. For instance, industry primarily relies on semiconductor pressure sensors for pressure measurement at elevated temperatures. But their maximum operating temperature is limited to only 482°C, which can easily be exceeded in many industrial environments. Also, thermal expansion mismatch between different materials can cause changes in temperature to appear as changes in pressure. What's more, they exhibit very short lifetimes and rather poor reliability in corrosive environments.^[4]

Fortunately, the miniature optical fiber tip pressure sensor presented in this thesis is a good candidate to solve the above problems. If packaged properly, it can be reliably used in high temperature, high pressure, and corrosive environments. In addition, it is chemically inert, very small, insensitive to temperature changes, immune to electromagnetic interference, easily manufacturable and inexpensive.

1.2 Miniaturized Sensing Technology

Many miniaturized sensing principles use micro-electromechanical systems (MEMS) technology and optical detection. MEMS-based sensors offer a reduction in size to the range 1mm to 1μm. MEMS is the integration of mechanical elements, sensors, actuators, and electronics on a common silicon substrate through microfabrication technology. While the electronics are fabricated using integrated circuit (IC) process sequences (e.g., CMOS, Bipolar, or BICMOS processes), the micromechanical

components are fabricated using compatible "micromachining" processes that selectively etch away parts of the silicon wafer or add new structural layers to form the mechanical and electromechanical devices. ^[5]

1.2.1 MEMS Sensors

1.2.1.1 Piezoresistive Sensors

At present, the most widely developed instrumentation for dynamic pressure measurement is based on piezoresistive silicon sensors, comprising a silicon diaphragm containing an array of strain gauges on a silicon chip approximately 1mm square. Piezoresistance of a semiconductor can be described as the change in resistance caused by an applied strain. Silicon is a perfect crystal and does not become permanently stretched. A change in pressure (mechanical input) is converted to a change in resistance (electrical output). The resistors can be connected in a Wheatstone bridge arrangement. The change in resistance depends on its orientation with respect to the crystalline direction of the silicon material. ^[6]

1.2.1.2 Capacitive Sensors

Microengineered capacitive pressure sensors can be simply formed by bonding conductive wafers together with a dielectric spacer, or by using silicon on insulator (SOI) wafers and sealing a sacrificially etched cavity. In addition, a number of dedicated capacitive interface chips are now available allowing simple interfacing. A change in pressure (mechanical input) is converted to a change in capacitance (electrical output). The advantages of capacitive sensors compared with piezoresistive devices are perceived as: high temperature operation (>125°C); low power consumption; high overpressure capability and high resistance to pressure shocks; low temperature coefficient and ease of packaging.

1.2.1.3 Frequency Dependent Capacitive Sensors

Capacitive pressure sensors combined with passive telemetry are very attractive. The module employs a MEMS silicon capacitive pressure sensor performing pressure to frequency conversion and a miniature on-board coil loop serving as the inductor for the LC tank and also a transmitting antenna. The output signal is frequency dependent, which makes the resonant solution more immune to noise than both the capacitive and the piezoresistive technique.

1.2.2 Fiber Optic Sensors

Although several MEMS sensing mechanisms using capacitive and piezoresistive effects are suitable for mass production, the fabrication process is usually complicated and requires expensive semiconductor equipment and devices. Compared with the electrical counterparts, optical fiber pressure sensors are in the same size range and possess many other potential advantages.^[7] The utilization of optical fibers in the field of sensing dates back well over thirty years. Generally speaking, optical fiber sensors are tools to produce a parameter-related optical signal through physical, chemical, biological, or other measurand interactions with light guided in an optical fiber or guided to an interaction region by an optical fiber.

In addition to a high sensitivity to a wide range of measurands with a wide dynamic range, optical fiber sensors can provide numerous operational benefits. They are electromagnetically passive and immune to electromagnetic interference, which make them suitable for operation in high and variable electric field environments. They are chemically and biologically inert because of the biocompatibility of the basic material of fiber - silica. Also, the tiny size of fiber, generally on the order of hundreds of microns in diameter, makes the fiber sensors physically small and light in weight. Distributed measurement capability, in which the measurand can be determined as a function of position along the length of a fiber simply by interrogating the fiber from one end, is an extremely powerful tool and provides access to an important array of niche applications. Additionally, the long distance transmission capability of optical fiber enables remote sensing, kilometers away from the monitoring station, another unique and extremely valuable feature. This is especially beneficial to many applications where the presence of powering wires and electrical components at the sensing site could be a source of hazards, or the presence of a severe electromagnetic interference environment makes reliable data transmission over electrical wires impossible. If the optical fiber is also the sensing element, coupling losses are greatly reduced and an improved sensitivity can be achieved. The possibility of multiplexing sensors in a fiber-connected network is also very attractive for multi-point sensing applications.

1.2.2.1 Categories of Optical Fiber Sensors

In the early 1970s researchers realized that light guided by an optical fiber could be modulated by direct physical perturbation and that optical fiber sensors can thus be obtained.^[7] Ever since then, various sensors, including magnetic, acoustic, thermal, acceleration, rotation, etc, have been developed. Figure 1-2 shows the primary application areas for fiber sensor technology.^[8]

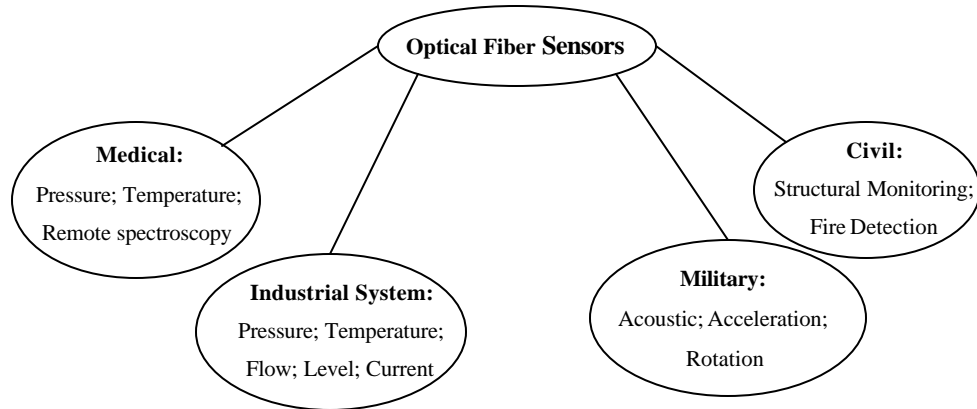


Figure 1-2 Application areas for optical fiber sensors

- **Intrinsic and Extrinsic Sensors**

According to the sensing element, optical fiber sensors can be classified into extrinsic and intrinsic sensors.^[2] In extrinsic sensors, a sensing element external to the fiber is used to modulate the optical signal. The light leaves the fiber, passes through some external transduction element, and is then coupled back into a fiber. The function of the fiber is to carry the light in and out of this sensing element. This style offers many ways to achieve the sensing desired, because one can add things that may be more sensitive than the fiber alone.

Intrinsic sensors utilize a part of the fiber as the sensing element where the optical signal traveling through it is modulated with changes in the measurand. Intrinsic sensors generally provide compactness, avoiding coupling between the fiber ends at the sensing site. However, this typically involves measurand-induced excess loss in the sensing fiber region.

- **Intensity and Phase Modulated Sensors**

According to the means of sensing, optical fiber sensors are mainly classified into intensity and phase modulated (interferometric) sensors. In the former class the physical perturbation acts directly to modulate the intensity of the light; and a direct detection scheme can be used to determine changes in the measurand. The advantages of intensity sensors are the simplicity of construction. The intensity based sensor requires more light and therefore usually uses large core multimode fibers.

In an interferometric sensor, changes in the measurand modulate the phase of the optical signal and an interferometric detection scheme is needed. The interferometric sensors offer theoretically orders of magnitude improvement in sensitivity.

A number of self-referenced fiber sensor configurations have been reported. Changes

in the measurand induce changes in the characteristics of the spectral modulation. The most commonly used approach involves the use of an external Fabry-Pérot cavity. [8]

1.2.2.2 Fabry-Pérot Theory

The Fabry-Pérot interferometer, consisting of two parallel flat semi-transparent mirrors separated by a fixed distance, has been utilized as a sensor for a long time. Its capability of transferring wavelength encoded information into an intensity signal makes it superior to its counterparts for higher stability and resolution. Recent developments enabling such a structure to be formed conveniently at the fiber end combines the advantages of both optical fiber and Fabry-Pérot sensors. Strong sensing ability, easy fabrication, miniaturized size and low cost, are only a few of its advantages. These factors have motivated much research and development in the Fabry-Pérot optical fiber sensor technology, which stands now as a well-established branch of photonics applications. [9]

1.3 Organization of the Thesis

In this research, we designed and fabricated a miniature optical fiber tip pressure sensor with a diameter of only 125 μm . Its intrinsic advantages include

- Ultra small size (125 μm in diameter)
- Very high resolution and accuracy
- Extremely low thermal expansion
- Material biocompatibility (silica)
- Electrical passivity
- Immunity to electromagnetic interference (EMI)
- Disposability (ecologically safe)
- Low cost
- Harsh environment endurance
- High temperature endurance (300°C)
- High frequency response (150kHz)
- Chemically and electrically inert

These unique characteristics permit the sensor to function well in harsh industry and medical environments.

As presented in the following paragraphs, this thesis is organized into five chapters.

Chapter 1: Need for miniature pressure sensors. This chapter covers the current methods of detection and their problems, categories of optical fiber sensors and their advantages.

Chapter 2: Sensor design. This chapter gives a detailed description of the considerations for the sensor design, including the Fabry-Pérot

theory, diaphragm-based sensor principle, and coefficients of the cavity and diaphragm selection.

- Chapter 3:** Sensor fabrication. This chapter presents the fabrication process in detail, with emphasis on the cavity and diaphragm manufacture.
- Chapter 4:** Laboratory testing and performance analysis. After the construction of the pressure testing system is introduced, the sensor's static and dynamic performance is analyzed, including sensitivity, repeatability, hysteresis, temperature dependence and high temperature stability.
- Chapter 5:** Field test results. The sensor is further tested on a jet engine. Packaging, test scheme, and fieldwork details are included. Data is analyzed and compared with a commercial Kulite reference sensor.
- Chapter 6:** Conclusions and future work. This chapter summarizes the entire thesis and also suggests areas of future research that would allow this sensor system to be deployed in commercial industry.

Chapter 2 Sensor Design and System Structure

As mentioned in Chapter 1, optical sensors are mainly categorized as either intensity or phase modulated. One difficulty with intensity-modulated sensors is that variations in transmission losses cause too much error in the steady-state measurement. For applications that require an absolute measure of a parameter with high accuracy, it is clear that an intensity-modulated sensor will not suffice. Due to the high accuracy and resolution of interferometric sensors, they are more desirable and have become the primary trend in the recent years. For these reasons we have concentrated our efforts on the development of an interferometric sensor system.

Fundamentally, all interferometers operate by modulating the optical path length or phase of one portion of the optical input with respect to another portion. The output of the sensor depends upon the characteristics of the input light, and the optical configuration of the interferometer. Generally, the output light consists either of a series of pulses whose position in time depends upon the parameter being sensed, or a wavelength modulated signal. ^[8]

Compared with other interferometric sensing schemes, such as Mach-Zehnder, Michelson or Sagnac configurations, fiber optic sensors based upon the Fabry-Pérot interferometer have several distinct advantages. They have been shown to provide high sensitivity, ‘point’ sensing, polarization independence, and multiplexing capacity. ^[8] Also, only one fiber is required, which allows the sensor to be compact. In addition, the sensor head is made of fused silica, which provides good temperature stability. Furthermore, the sensor is insensitive to intensity variation in the lead-in fiber and can be made quite rugged.

Optical fiber pressure sensors typically have a Fabry-Pérot etalon cavity optically coupled to the fiber. The etalon is constructed so that applied force or hydrostatic pressure causes the etalon cavity length to change. The etalon cavity length is remotely monitored optically. For example, the reflectivity of the etalon at a specific wavelength or group of wavelengths can be monitored. In this way, pressure is measured optically. ^[9]

Conventional fiber optic pressure sensor designs are typically not suitable for applications in extreme environments. The presence of certain metals in a sensor, for example, precludes use at high temperature and in corrosive environments. Also, thermal expansion mismatch between different materials can cause changes in temperature to appear as changes in pressure.

It would be an advance in the art to provide an optical fiber pressure sensor that can be used at high temperatures and in corrosive environments. It would be particularly beneficial for the pressure sensor to be chemically inert, very small, insensitive to temperature changes, easily manufacturable and inexpensive. Our optical fiber pressure sensor can fulfill the above requirements. It consists of a hollow fiber tube connecting a piece of standard optical fiber and a pressure-sensitive diaphragm. The fiber endface and diaphragm define an etalon cavity. The length of the etalon cavity changes under applied pressure.

In the following paragraphs, the Fabry-Pérot interference theory is reviewed, then the principle of diaphragm based pressure sensors is introduced, design considerations of our fiber tip pressure sensor are presented, finally the fabrication and testing systems are illustrated.

2.1 Fabry-Pérot Interferometer Theory

The Fabry-Pérot interference device was first advanced in the late 19th century by two young French physicists at the University of Marseille, Alfred Pérot and Charles Fabry.^[3] The interference was caused by waves successively reflected between two accurately parallel thinly silvered plane glass plates. The underlying principles were developed, several experimental methods were introduced, and the potential applications were illustrated. The reliability of the equipment and the ease of interpretation quickly made their mark.^[9]

As optical fiber technology develops, more and more researchers realize the combination of optical fiber sensing techniques and Fabry-Pérot interference theory can introduce many advantages such as compactness, high-sensitivity and high accuracy. Recent rapidly developing MEOMS (Micro-Electro-Optical-Mechanical-Systems) technology drives this combo-technology forward and makes it the trend in the sensing research area.

2.1.1 Geometric Ray Analysis

A Fabry-Pérot interferometer consists of two glass plates whose separation can be adjusted. The field distribution over the plates, which requires cavity mode analysis, is not usually considered. For spectroscopic purposes the geometric treatment is usually sufficient.^[10]

Consider the plane waves successively reflected between two parallel surfaces, as shown in Figure 2-1. The relative amplitude coefficients of the reflected set of beams a, b, \dots and transmitted beams α, β, \dots are shown. Assume the electrical vector of the incident wave is of unit amplitude, linearly polarized either parallel or perpendicular

to the plane of incidence.

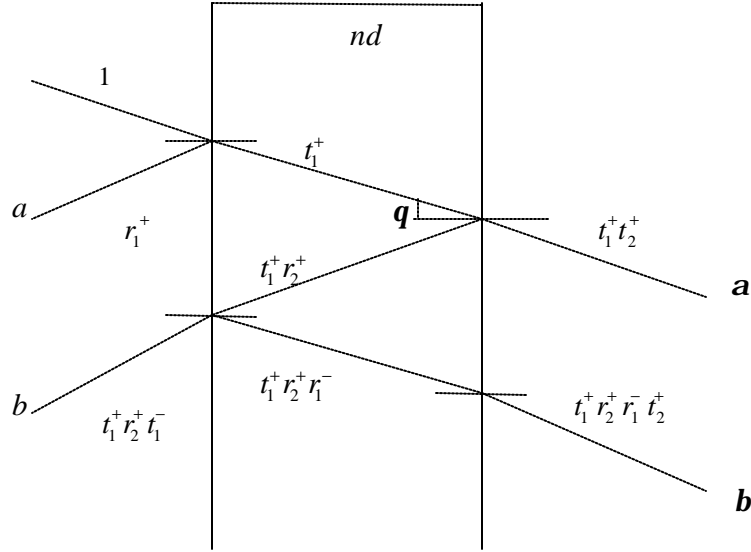


Figure 2-1 Schematic of Fabry-Pérot interference

For successive reflections, the optical delay gives an additional phase difference f , which is:

$$j = 2\pi(2nd \cos q) / \lambda_0 \quad (2 - 1)$$

n : The effective refractive index of the interspace

λ_0 : The wavelength of the light in vacuo

q : The angle of incidence of the beams on the surfaces from within the interspace

d : The distance between the two surfaces

From Fig. 2.1.1-1, we can see that the beams form geometrical progressions with the same factor $r_1^- r_2^+ e^{ij}$. The amplitude $E_t(m)$ of the resultant electrical vector of the first m transmitted beams is given by

$$\begin{aligned} E_t(m) &= t_1^+ t_2^+ \left[1 + r_1^- r_2^+ e^{ij} + \dots + (r_1^- r_2^+)^{m-1} e^{j(m-1)} \right] \\ &= t_1^+ t_2^+ \left[1 - (r_1^- r_2^+)^m e^{jm} \right] / (1 - r_1^- r_2^+ e^{ij}) \end{aligned} \quad (2 - 2)$$

For an infinite number of beams as $m \rightarrow \infty$, E_t becomes

$$E_t \rightarrow E_t(\infty) = t_1^+ t_2^+ / (1 - r_1^- r_2^+ e^{ij}) \quad (2 - 3)$$

The corresponding transmitted intensity I_t is the square modulus $E_t E_t^*$, so

$$I_t = |t_1^+ t_2^+|^2 / \left(1 + |r_1^- r_2^+|^2 - 2|r_1^- r_2^+ \cos y \right) \quad (2 - 4)$$

Here,

$$\mathbf{y} = \mathbf{j} + \mathbf{e} \quad (2-5)$$

Where \mathbf{e} is the correction for phase changes on reflection given by

$$\mathbf{e} = \arg r_1^- + \arg r_2^+ \quad (2-6)$$

When the surfaces are identical uncoated dielectrics, the coefficients r and t are real
For a single surface,

$$\begin{aligned} t^+ t^- &= T \\ r^+ &= -r^- \\ r^{+2} &= r^{-2} = R \\ R + T &= 1 \end{aligned} \quad (2-7)$$

R : The surface intensity reflection coefficient

T : The surface intensity transmission coefficient

For identical dielectrics,

$$\begin{aligned} \mathbf{e} &= 0 \\ t_2^+ &= -t_1^- \\ r_2^+ &= -r_1^- \end{aligned} \quad (2-8)$$

The energy transmission coefficient for the pair of surfaces is

$$\begin{aligned} I_T &= T^2 / (1 + R^2 - 2R \cos \mathbf{j}) \\ &= T^2 / [(1 - R)^2 + 4R \sin^2(\mathbf{j} / 2)] \\ &= \frac{T^2}{(1 - R)^2} \left(\frac{1}{1 + [4R / (1 - R)^2] \sin^2(\mathbf{j} / 2)} \right) \\ &= [T / (1 - R)]^2 [1 + F \sin^2(\mathbf{j} / 2)]^{-1} \\ &= [T / (1 - R)]^2 A(\mathbf{j}) \end{aligned} \quad (2-9)$$

where

$$F = 4R / (1 - R)^2 \quad (2-10)$$

$A(\mathbf{j})$: The Airy shape function.

Similarly, the amplitude $E_r(m)$ of the electric al vector of the first m reflected beams is given by

$$\begin{aligned}
E_r(m) &= r_1^+ + t_1^+ t_1^- r_2^+ e^{ij} \left[1 + r_1^- r_2^+ e^{ij} + \dots + (r_1^- r_2^+)^{m-2} e^{j(m-2)j} \right] \\
&= r_1^+ + \left\{ t_1^+ t_1^- r_2^+ e^{ij} \left[1 - r_1^- r_2^+ e^{j(m-1)j} \right] \right\} / (1 - r_1^- r_2^+ e^{ij})
\end{aligned} \quad (2-11)$$

For an infinite number of beams as $m \rightarrow \infty$, E_r is given by

$$E_r \rightarrow E_r(\infty) = r_1^+ + (t_1^+ t_1^- r_2^+ e^{ij}) / (1 - r_1^- r_2^+ e^{ij}) \quad (2-12)$$

For the two identical dielectric surfaces,

$$\begin{aligned}
E_r &= r_1^+ - t_1^+ t_1^- r_1^+ e^{ij} / (1 - r_1^{+2} e^{ij}) \\
&= \sqrt{R} (1 - R e^{ij} - T e^{ij}) / (1 - R e^{ij}) \\
&= \sqrt{R} (1 - e^{ij}) / (1 - R e^{ij})
\end{aligned} \quad (2-13)$$

The intensity of the reflected beam is given by

$$\begin{aligned}
I_R &= E_r E_r^* \\
&= R (2 - 2 \cos \mathbf{j}) / (1 + R^2 - 2R \cos \mathbf{j}) \\
&= 4R \sin^2(\mathbf{j}/2) / \left[(1 - R)^2 + 4R \sin^2(\mathbf{j}/2) \right] \\
&= F \sin^2(\mathbf{j}/2) [1 + F \sin^2(\mathbf{j}/2)]^{-1}
\end{aligned} \quad (2-14)$$

Examination of the expressions for the transmitted and reflected patterns shows that they are complementary in that

$$I_T + I_R = \left[T^2 / (1 - R)^2 + F \sin^2(\mathbf{j}/2) \right] / [1 + F \sin^2(\mathbf{j}/2)]^{-1} \quad (2-15)$$

When there is no surface absorption,

$$R + T = 1 \quad (2-16)$$

$$I_T + I_R = 1 \quad (2-17)$$

2.1.2 Fringe Patterns

By considering I_T and I_R as a function of phase difference \mathbf{j} , the shape of the fringe patterns can be examined.^[12]

For typical dielectrics at near-normal incidence, R is small ($R \ll 0.1$), accordingly, from (2-10), F is small. Then, (2-14) can be simplified as

$$\begin{aligned} I_R &\approx F \sin^2(\mathbf{j}/2) \\ &= F(1 - \cos \mathbf{j})/2 \end{aligned} \quad (2-18)$$

From (2-17):

$$\begin{aligned} I_T &= 1 - I_R \\ &\approx 1 - F \sin^2(\mathbf{j}/2) \\ &= 1 - F(1 - \cos \mathbf{j})/2 \end{aligned} \quad (2-19)$$

When multiple layers of thin dielectric films or partially transparent metal films are used, high reflectivities at near-normal incidence are achieved. Providing that the two surfaces of the plate are identical, $r_2^+ = r_1^-$, the intensity transmission coefficient (2-9) is modified

$$\begin{aligned} I_T &= [T/(1-R)]^2 / [1 + F \sin^2(\mathbf{j}/2)] \\ &= [(1-R-A)/(1-R)^2] / [1 + F \sin^2(\mathbf{y}/2)] \\ &= [1 - A/(1-R)]^2 A(\mathbf{y}) \end{aligned} \quad (2-20)$$

where the surface reflectivity from within the interspace is

$$R = |r_2^+|^2 = |r_1^-|^2 \quad (2-21)$$

$$\mathbf{y} = \mathbf{j} + \mathbf{e} \quad (2-22)$$

$$\mathbf{e} = 2 \arg r_2^+ \quad (2-23)$$

$$R + T + A = 1 \quad (2-24)$$

For metal films, A is the fraction of light absorbed by the metal.

For dielectric films, A is the fraction of light due to the losses by scattering.

Thus for low reflectivities the fringes are broad and only in the reflected system do the intensity minima approach zero. For increasing values of R, the value of F increases very quickly, and the fringes become sharper. Thus, the transmitted fringe pattern consists of sharp bright fringes against a greatly reduced background, while the reflected pattern is one of narrow dark fringes on a bright background, as shown in Figure 2-2.

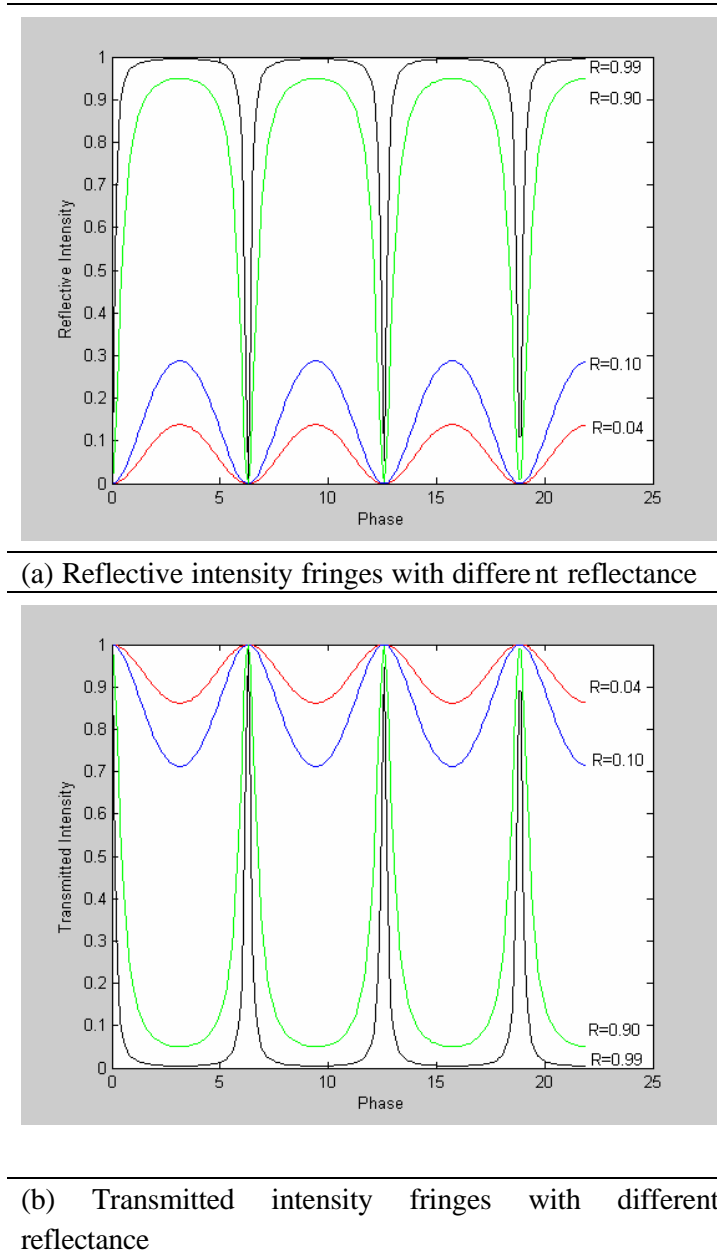


Figure 2-2 Reflective and transmitted intensity fringe patterns

2.1.3 Two-Beam Model

When the reflectivity is low, the response is a periodic function similar to a two-beam interferometer: ^[13]

$$\begin{aligned}
 I &= E_1^2 + E_2^2 + 2E_1E_2 \cos\left(\frac{4\pi nd}{\lambda} + j_0\right) \\
 &= I_1 + I_2 + 2\sqrt{I_1I_2} \cos\left(\frac{4\pi nd}{\lambda} + j_0\right)
 \end{aligned}
 \tag{2 - 25}$$

E_1, E_2 : the magnitudes of the electrical fields of the reflected light

n : The effective refractive index of the medium

d : Cavity length

λ : Wavelength

j_0 : Initial phase

I_1, I_2 : are the light intensity received at the photodetector.

2.2 Principles of Diaphragm-based Pressure Sensors

2.2.1 Theory of Diaphragm Based Pressure Sensor

The configuration of an extrinsic Fabry-Pérot interferometric (EFPI) sensor is shown in Figure 2.3. A single mode silica optical fiber transmits light from a laser diode to the sensor element through a 2×2 coupler. In the sensor head, the laser light is partially reflected and partially transmitted across the gap formed by the end of the input fiber and a diaphragm. The light reflected from the first interface (the input fiber end) and the light reflected at the second interface (the endface of the diaphragm) interfere with each other to modulate the returned optical spectrum. A sinusoidal interference signal can be obtained at the photo-detector due to differential phase changes between the two light beams as a result of changes in the EFPI sensor cavity spacing.

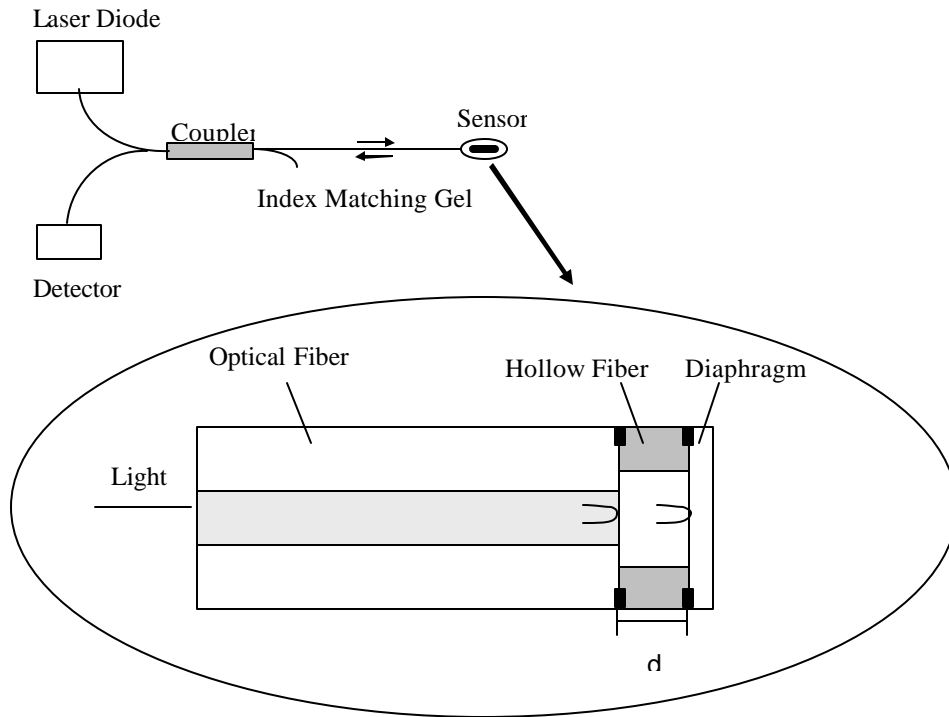


Figure 2-3 Configuration of Extrinsic Fabry-Pérot Interferometer (EFPI)

As we discussed in 2.1.3, the detected photodiode signal current can be shown as a function of the phase difference between the two reflected optical fields and is given by:

$$I = I_1^2 + I_2^2 + 2I_1I_2 \cos(\mathbf{f}_1 - \mathbf{f}_2) \quad (2 - 26)$$

where I_1 and I_2 are the light intensities reflected at the fiber end and the diaphragm respectively, and $\mathbf{f}_1 - \mathbf{f}_2$ is the relative phase difference between the two light signals. If we assume I_1 and I_2 to be equal, equation (2.2.1-1) can be rewritten as

$$\begin{aligned} I &= 2I_0 \left[1 + \cos\left(\frac{4\mathbf{p}d}{\mathbf{l}}\right) \right] \\ &= 2I_0 \left[1 + \cos\left(\mathbf{f}_0 + \frac{4\mathbf{p}\Delta d}{\mathbf{l}}\right) \right] \end{aligned} \quad (2 - 27)$$

where d denotes the length of the cavity, Δd is the airgap change, \mathbf{l} is the laser diode wavelength of operation in free space, and \mathbf{f}_0 is the phase constant related to initial airgap.

When the applied pressure changes, the diaphragm will deform accordingly, resulting in an air-gap change:

$$\Delta L = \frac{3(1-\mu^2)R^4}{16Eh^3} \Delta P \quad (2 - 28)$$

where ΔP is the pressure variation, R is the radius of the diaphragm, E is the Young's modulus for the material, μ is Poisson's ratio and h is the thickness of the diaphragm. Therefore the airgap change is linearly dependent on the applied pressure. Resolving the air-gap change from the spectral shift can thus provide information about pressure. ^[13]

2.2.2 Sensor Coefficient Design

2.2.2.1 Sensitivity

Sensitivity (d_{diap}), one of the most important performance indexes of a pressure sensor, is defined by the ratio of the deflection to the pressure applied ^{[14] [15]} The diaphragm structure is shown in Figure 2-4. The out-of-plane deflection of the diaphragm y is given by

$$y = \frac{3(1-\mu^2)p}{16Eh^3} \times (r^2 - a^2) \quad (2 - 29)$$

r : The radius of free area of the diaphragm (μm)

h : The thickness of the diaphragm (μm)

μ : The Poisson's ratio

E : The Young's modulus of the diaphragm material

p : The applied pressure (psi)

a : The radius position of the interest

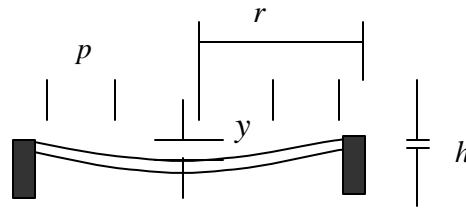


Figure 2-4 Diaphragm structure

In the configuration of Figure 2-4., the fiber is centered with respect to the diaphragm, $a=0$, so d_{diap} is given by

$$d_{diap} = \frac{y}{p} = \frac{3(1-\mu^2)}{16Eh^3} \times r^4 \quad (2 - 30)$$

The parameters of fused silica, the optical fiber material, are listed in Table 2-1. [16]
For a fused silica pressure sensor,

$$d_{diap} = 1.71 \times 10^{-8} \times \frac{r^4}{h^3} \quad (\mu\text{m/psi}) \quad (2-31)$$

Table 2-1 Properties of fused silica (at 25°C)

Density	w	2.202×10^3	Kg / m^3
Young's Modulus	E	73.73×10^9	Pa
Poisson's Ratio	m	0.17	-

2.2.2.2 Diaphragm Frequency Response

Another important factor we have to consider when dynamic pressure measurement is required is the frequency response. In addition to the vibration modes being symmetrical with respect to the center, a diaphragm can have modes in which diameters are nodal lines – along which the deflection during vibration are zero. This can be investigated by pouring powder on a vibrating diaphragm. [14] [15] [16] While in our applications, only the fundamental mode is considered and analyzed.

When the diaphragm is a free vibrating circular plate clamped at its edge, its natural frequency f_{mn} (Hz) is given by [6]

$$f_{mn} = \frac{a_{mn}}{2\pi r^2} \times \sqrt{\frac{Dg}{hw}} \quad (2-32)$$

$$D = \frac{Eh^3}{12(1-m^2)} \quad (2-33)$$

a_{mn} : A constant related to the vibrating modes of the diaphragm

g : The gravitational constant

w : The density of the diaphragm material

D : The flexural rigidity of the diaphragm

μ : The Poisson's ratio

E : The Young's modulus of the material

r : The radius of free area of the diaphragm (μm)

h : The thickness of the diaphragm (μm)

Table 2-2 Values of a_{mn}

a_{mn}	n=0	N=1	n=2
m=0	10.21	21.22	34.84
m=1	39.78	60.82	84.58
m=2	88.90	120.12	153.76

By inserting a_{00} and the coefficients of fused silica into (2 – 32) and (2 – 33), the fundamental frequency response can be obtained by

$$f_{00} = 2.749 \times 10^9 \times \frac{h}{r^2} \quad (2 - 34)$$

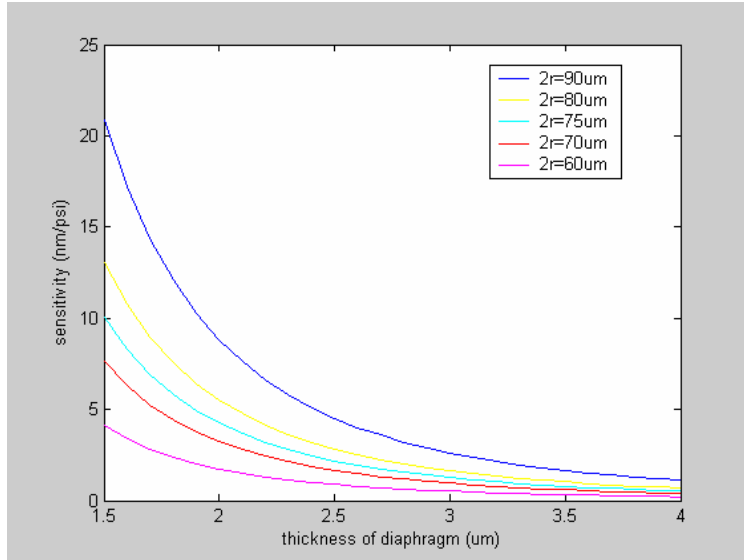
where h and r are in microns.

As indicated by Equation (2 - 34), the frequency response is proportional to the thickness of the diaphragm and inversely proportional to the square of the effective diaphragm radius.

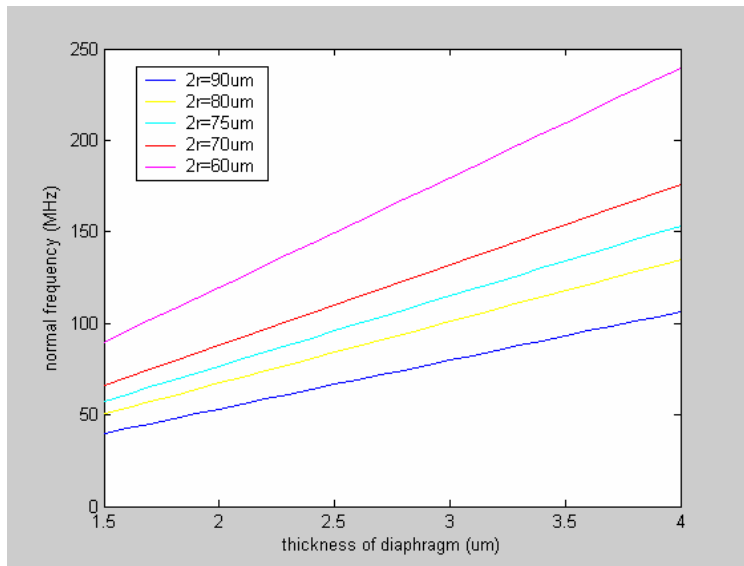
2.2.2.3 Sensor Dimension Design

In order to design a pressure sensor for measuring static and dynamic pressure in a high pressure background with high sensitivity, the cavity length, freestanding diameter and diaphragm thickness are three key parameters. In our case, the configuration is built on the tip of the fiber; so the freestanding diameter of the diaphragm is determined by the inner diameter of the hollow fiber tubing, which forms the cavity.

As presented in 2.2.2.1 and 2.2.2.2, high frequency response and high diaphragm sensitivity are two opposing requirements and have to be considered collectively. From Figure 2-5(a), we can see that the sensitivity is highly dependent on the diaphragm's thickness and radius. As illustrated in Figure 25, when the radius is fixed, the sensitivity decreases as the thickness increases. When the thickness is constant, the sensitivity increases with increasing diaphragm radius. Thus, in order to obtain high sensitivity, the thinner and the larger the diaphragm, the better.



(a) Sensitivity versus r and h



(b) Frequency response versus r and h

Figure 2-5 Relationship between sensor performance and r and h

On the other hand, the frequency response is proportional to the thickness and reciprocal to the square of the radius. As shown in Figure 2-5(b), when the radius of the diaphragm increases, the frequency response decreases. Generally, in order to obtain a flat response within a specific frequency range, the function point should be set far lower than the natural frequency. In order to measure dynamic pressure at high frequency, a high natural frequency is desired. So a thicker and smaller diaphragm is preferred. This is contrary to the requirement of high sensitivity. As a consequence, a tradeoff has to be made to satisfy both requirements.

In addition, it is a rule of thumb that the maximum usable frequency should be taken

to be one fifth or one seventh of its natural frequency. ^[15] In order to obtain a flat frequency response from DC to 150 kHz, let $f_{\infty} > 750$ kHz.

Diaphragm thickness and freestanding diameter will also influence the operating pressure range of the sensor. A relatively thick diaphragm and/or small freestanding diameter are needed for sensing high pressures. In order to obtain the linear response of the diaphragm, the maximum deflection due to applied pressure should not be more than 30% of the thickness of the diaphragm. For example, with a freestanding diameter of about 75 microns, for a sensing pressure in the range of about 5000-10,000 PSI, the diaphragm can be about 4.90- 5.85 microns thick; for sensing pressures in the range of about 1 – 200 PSI, the diaphragm can be about 0.585 – 2.19 microns thick.

To align with the fiber and increase the mechanical strength, the outside diameter is preferred to be the same diameter as the SMF. In our test, a 75 μ m inner diameter hollow fiber was selected. Its outside diameter is 125 μ m, the same as the SMF. So the wall thickness is $\frac{(125 - 75)}{2} = 25\text{mm}$. This 25 μ m shoulder ensures a robust splicing effect to bond the diaphragm. At the same time, combined with a thin diaphragm of about 2.5 μ m, the sensor can achieve high sensitivity (1-2nm/psi) to meet the requirement. The cavity length (and tube length) can be in the range of about a few microns to millimeters, for example. More typically, the cavity length is in the range of about 5-60 microns.

2.2.3 Material Selection

2.2.3.1 Single Mode EFPI Sensor

In our research, we focused on single mode diaphragm-based sensors. There are several reasons for choosing single mode fiber.

First of all, from the sensor fabrication perspective, it is easier to make a sensor from a single mode fiber than from a multimode fiber, when the signal visibility is the same. The reason lies in the fact that there is more than one mode reflected from the diaphragm if a multimode fiber is used. If the mode reflected from the diaphragm does not excite the original mode, the interference fringe visibility will be damped

Secondly, from the viewpoint of measurement capability, the light source for a single mode fiber system has a narrower spectral width. Accordingly, the single mode fiber system has a greater coherence length, and hence provides larger dynamic range for pressure sensing.

Thirdly, from the signal detection standpoint, single mode fiber components, such as long wavelength filters, are more readily available because of the development of single mode fiber communications.

Last but not the least, for future practical use, the sensors made by single mode fiber can be used for long-distance monitoring. As a transmission line, single mode fiber has less transmission loss compared with multimode fiber and has been widely deployed all over the world.

2.2.3.2 All Fused Silica Material Selection

In my work, fused silica was chosen for the pressure-sensitive sensor diaphragm. Fused silica has many advantages in high temperature applications due to its inertness and stability at extremely high temperatures; and excellent transparency. In addition, fused silica offers an extremely low coefficient of thermal expansion and high Young's Modulus, which makes it immune to stress effects from thermal shock or thermal gradients. Furthermore, fused silica remains elastic (no observable creep or hysteresis) up to temperatures very near its annealing point of 1100°C. Also, our all fused silica miniature fiber tip sensor can be used in medical and biological environments, because fused silica is a biocompatible material.

Finally, fused silica is widely available, and easy to fabricate into specialized components at modest cost. Most commercial optical fiber and hollow fiber tubing are made of fused silica, and they are of low cost. To decrease the temperature effect due to different materials, it is preferable to select the same material - fused silica for diaphragms. In our experiment, to reduce the cost, commercial optical fibers are used for diaphragms.

2.3 Signal Processing and System Introduction

Signal demodulation is an important part of sensor fabrication and performance testing. Test details will be analyzed in Chapter 4. Here we briefly introduce the equipment utilized in our work.

2.3.1 Micron Optics Component Testing System (CTS)

In my research, the fabrication and static pressure testing processes were monitored by the Component Testing System (CTS) shown in Figure 2.3.1-1. It is a high resolution swept laser interrogator. It contains a very fast, high signal-to-noise ratio swept laser, high dynamic range detectors and amplifiers, high speed, simultaneously sampling data acquisition, and a real time operating system to tie it all together and display data to an LCD. The source is a mode-locked Er-doped fiber ring laser whose

maximum average power is 0dBm, and the peak pulse energy is 0.1nJ. It continuously sweeps 5 times per second in the wavelength range between 1520nm and 1570nm.



Figure 2-6 Photo of Component Testing System (CTS) used to monitor fabrication and static testing processes.

2.3.2 White Light System

For dynamic pressure testing, the CTS cannot respond fast enough for the signal demodulation. Fortunately, our center has fabricated a white light system combining a 1310nm LED source and tunable optical filter, which can accomplish the dynamic task. A photo of the system is shown in Figure 2.3.2 1.

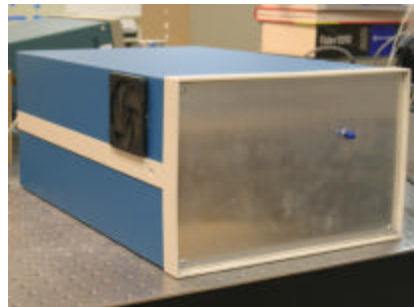


Figure 2-7 Photo of the white light system used for dynamic pressure testing.

Chapter 3 Sensor Fabrication

The miniature optical fiber tip pressure sensor is a diaphragm-based extrinsic Fabry-Pérot interferometric (EFPI) sensor. The fabrication includes fusion splicing a hollow tube to an endface of an optical fiber, and then cleaving the hollow tube and fusion splicing a diaphragm to the hollow tube. This method requires only a fusion splicer and cleaver for fabricating the pressure sensor. Optionally, the diaphragm thickness can be adjusted by exposing an exterior surface of the diaphragm to an etchant. This section introduces the essential sensor fabrication procedures.

Because the sensor is capable of operating under harsh environments such as high temperature and high pressure, using materials with very the same CTE (coefficient of thermal expansion) as that of optical fiber is very important to reduce thermally induced air-gap changes and failures. Ordinary single mode optical fibers are made of fused silica. It's very straightforward to use fused silica for the cavity and the diaphragm. Also fused silica can be micro-structured, preferably using standard lithography process (batch fabrication).^[17]

3.1 Sensor Structure

The optical pressure sensor has a short length of hollow tube bonded to an endface of an optical fiber. A pressure-sensitive diaphragm is bonded to the opposite end of the hollow tube. The fiber endface and diaphragm define an etalon cavity. The diaphragm deflects in response to applied pressure, impact, vibrations or acoustic waves, varying the etalon cavity length. The etalon cavity length is normally approximately equal to the length of the hollow tube. The fiber, hollow tube, and diaphragm are preferably made of the same material (e.g. fused silica or sapphire) and can all be bonded by fusion bonding at high temperature.^[18]

Figure 3-1 shows the basic schematic of the structure and Figure 3-2 gives the photograph of such structure.

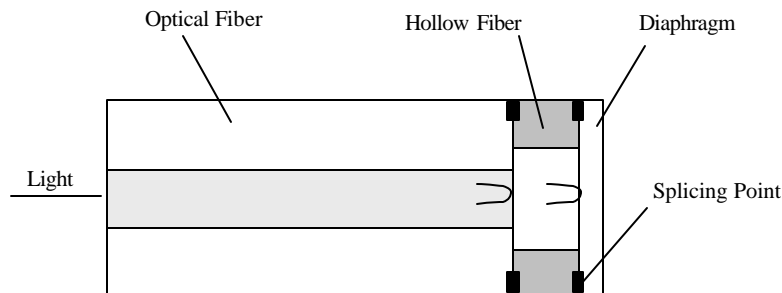


Figure 3-1 Schematic of the sensor structure

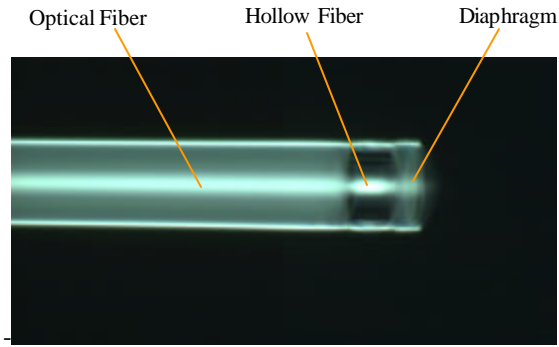


Figure 3-2 Photograph of the sensor structure

The diaphragm thickness can be in the range of about 1-100 microns; more typically the diaphragm thickness will be in the range of about 2-25 microns. The diaphragm must be thin enough to flex under applied pressure. The freestanding diameter will typically be the same as the inner diameter of the tube. Preferably, the freestanding diameter is equal to or greater than a diameter of the fiber core, though this feature is optional. The freestanding diameter can be in the range of about 575 microns, for example.

The cavity length (and tube length) can be in the range of about a few microns to millimeters, for example. More typically, the cavity length will be in the range of about 5-60 microns.

The fiber is preferably a conventional index-guided single mode optical fiber, but can also be a photonic-crystal fiber, a holey fiber, or a multi-mode fiber. The fiber can have a graded-index or step index, or any other light-guiding profile or structure.

Preferably, the fiber, tube and diaphragm are made of the same material, for example silica. Uniform material construction tends to reduce thermal expansion mismatch stress and associated temperature sensitivity. The fiber, tube and diaphragm can also be made of materials such as borosilicate glass or other glasses, sapphire, crystalline quartz or silicon. With fused silica components, the present sensor can operate at temperatures up to about 700°C. With a uniform sapphire construction, the maximum operating temperature can be increased to about 2000°C. Sapphire provides exceptional high temperature stability and high pressure performance.

The bonds between the fiber, tube, and diaphragm can be fusion bonds made by a fusion splicer. A fusion splice bond may be particularly well suited for use with fused silica and other glass components. The fusion splice bonds can be made with a conventional electric-arc fusion splicer, as described below. The fiber, tube, and diaphragm can also be bonded in other ways, for example by anodic bonding^[7], direct bonding, hydroxide bonding, agglutinating or by conventional adhesives such as sealing glasses or epoxy.

3.2 Fabrication Process:

Simply speaking, the fabrication process can be summarized as the following steps:

1. Splice a piece of hollow fiber tube to the cleaved end of a standard fiber.
2. Cleave the hollow fiber tube near the junction according to the cavity length requirement. The cavity length can be cleaved down to the order of micrometers under the inspection of a microscope or CCD.
3. Connect the diaphragm at the other end of the hollow fiber tube. The method can be splicing, agglutinating, heating, etc.
4. Control the diaphragm's thickness to the order of sub-microns by dipping the fiber head into HF acid of suitable concentration. This step is optional according to the requirement.

Cavity fabrication and diaphragm bonding are the two main steps during fabrication. The cavity is formed by cleaving and splicing a piece of hollow fiber. This is one of the unique features of this sensor.

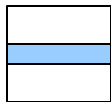
Diaphragm bonding can be realized by two methods: direct splicing and splicing with the stopper.

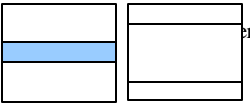
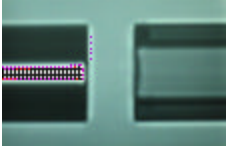
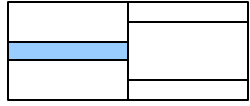
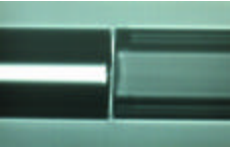
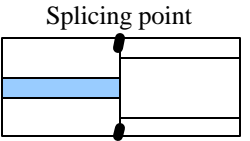
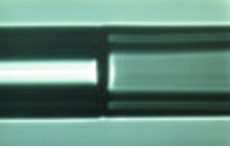
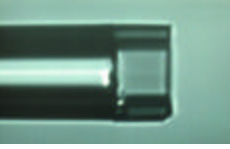
In this section, these processes are presented in detail.

3.2.1 Cavity Fabrication

Table 3-1 illustrates the 5 steps to fabricate the sensor cavity. The fusion splice may be formed in a conventional electric-arc fusion splicer. The hollow tube fiber may be fabricated from a hollow tube preform drawn into a fiber, in a manner analogous to making conventional optical fiber. Cleaving can be performed with a conventional diamond fiber cleaving tool. Cleaving is performed with high accuracy (within a few microns or less) so that the length of the bonded hollow tube is accurate. To achieve high accuracy, cleaving can be performed under a microscope. Alternatively, after cleaving the hollow tube can be shortened by chemical etching or polishing.

Table 3-1 Illustration of cavity fabrication

Description	Schematics	Photos
a) Cleave a piece of standard optical fiber.	<p>SM Fiber</p> 	

b) Cleave a piece of hollow fiber.		
c) Align these two fibers with a splicer.		
d) Splice the standard optical fiber with the hollow fiber.	 <p style="text-align: center;">Splicing point</p>	
e) Cleave the other end of the hollow fiber.		

During fabrication, we utilize the CTS to monitor the whole process. After calibration, the standard optical fiber is connected to the CTS. After each step of cleaving and splicing with the hollow fiber, the signal strength is observed to control the process within the error tolerance.

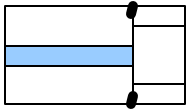
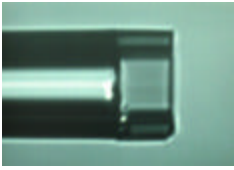
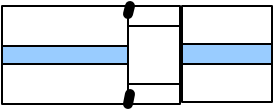
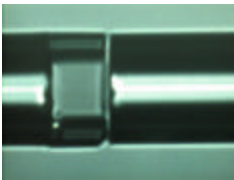
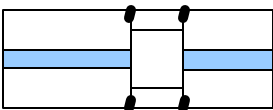
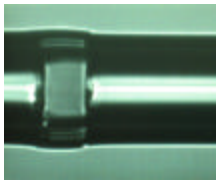
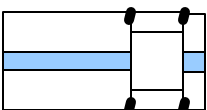
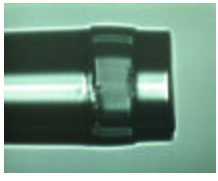
From the above description, we can see that the cavity fabrication is simple and direct. By utilizing a piece of hollow fiber, the whole process eliminates etching or other chemical methods. In addition, the cleaved fiber end is of much higher quality than the etched endface. By bonding a piece of rod or endface of fiber as a diaphragm, a Fabry-Pérot interferometer is formed.

3.2.2 Diaphragm Fabrication

3.2.2.1 Direct Diaphragm Bonding

A simple method for bonding the diaphragm to the cavity is shown in Table 3-2. A pure fused silica fiber is spliced with the cavity and then cleaved, leaving a ‘diaphragm’ on top of the cavity. In the illustration, a piece of optical fiber is fusion spliced to the hollow tube. The optical fiber can be a solid rod, a glass or fused silica fiber without any index variation or doping. The fusion splice is formed in a conventional electric-arc fusion splicer. The conventional optical fiber is cleaved, leaving the diaphragm attached to the hollow tube.

Table 3-2 Illustration of direct diaphragm bonding

Description	Schematics	Photos
a) Complete cavity formation.		
b) Align the hollow tube with a piece of fiber.		
c) Splice the hollow tube with the optical fiber.		
d) Cleave the optical fiber to form the diaphragm.		

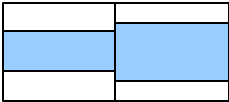
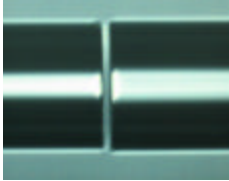
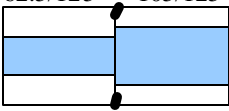
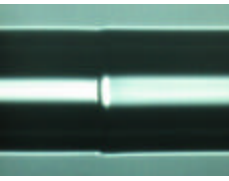
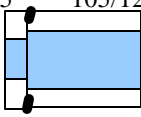
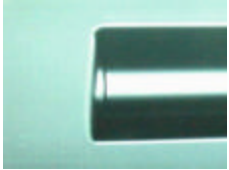
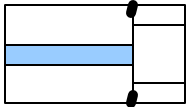
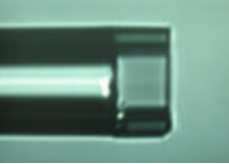
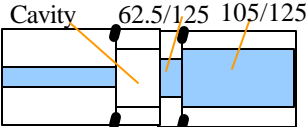
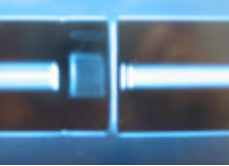
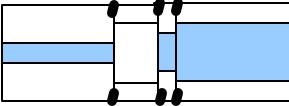
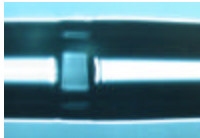
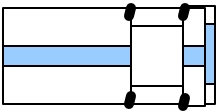
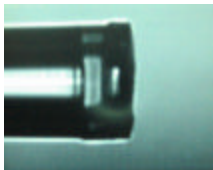
It is noted that the manufacturing process illustrated in Table 3-2 employs conventional and well-known fiber splicing and cleaving tools. Consequently, the present pressure sensor is simple and inexpensive to fabricate. Additionally, the materials required for construction (hollow tubes and solid fibers) are commercially available and very cheap. The present sensor has high mechanical strength and smooth optical surfaces that minimize optical scattering. These features are provided as a result of the cleave and splice manufacturing method. The sensor tends to have higher mechanical strength and lower scattering compared to fiber sensors made by etching or other destructive methods.

3.2.2.2 Diaphragm Bonding with an Etch Stop

Table 3-3 shows an alternative diaphragm formation with an etch stop. In this case, the etchant protection layer comprises the diaphragm. The etchant protection layer can be composed of fused silica, silicon nitride or other etch-resistant and transparent materials. The etchant protection layer can be formed by sputtered SiO_2 , or by fusion splicing a solid rod to the fiber and then cleaving the rod. The etchant protection layer protects the fiber endface from etchant used to remove the doped core. Without the

etchant protection layer, the diaphragm might be damaged or roughened when the diaphragm is thinned.

Table 3-3 Illustration of diaphragm bonding with an etch stop

Description	Schematics	Photos
a) Align a piece of 62.5/125 optical fiber with a piece of 105/125 fiber.	<p>62.5/125 105/125</p> 	
a) Splice the 62.5/125 optical fiber with the 105/125 fiber.	<p>62.5/125 105/125</p> 	
b) Cleave short the 62.5/125 fiber to the diaphragm thickness. The preformed diaphragm is formed.	<p>62.5/125 105/125</p> 	
c) Complete preformed cavity formation.		
d) Align the preformed cavity with the preformed diaphragm	<p>Cavity 62.5/125 105/125</p> 	
e) Splice the preformed cavity with the preformed diaphragm.		
f) Cleave the 105/125 optical fiber to form the diaphragm.		

3.3 Fabrication Tools

From the above description, we can see that cleaving and splicing are two key steps during fabrication. The splicer we use is the Sumitomo Type-36 Fusion Splicer, shown in Figure 3.3-1(a). Besides the general setup for the normal splicing, this splicer provides a manual mode to change the coefficients according to the specific requirements. The cleaver we utilize is a Fujikura CT-04B Fiber Cleaver, as shown in Figure 3.3-1(b). Since cleaving and splicing quality are highly related to the performance of the sensor, the cleaving process is investigated by a microscope. The splicing effect is investigated by Zeiss Axiovert 25 Microscope. The whole fabrication process is monitored by the Component Testing System (CTS). Additionally, in order to increase the sensor's sensitivity, we can use a wet-etching method to thinner the diaphragm. In the following paragraphs, the coefficient setup for the splicer, and the principle of wet-etching method are described.



a. Sumitomo Type-36 Fusion Splicer



b. Fujikura CT-04B Fiber Cleaver



c. Zeiss Axiovert 25 Microscope



d. CTS

Figure 3-3 Fabrication equipment setup

3.3.1 Coefficient Setup of the Splicer

Our fusion splicers can be set in auto or manual mode with adjustable splicing parameters. To minimize the temperature cross-sensitivity of the sensor, arc power and duration need to be carefully adjusted. In order to reduce the density and thus the amount of air trapped inside the cavity, fusion power should be high. On the other hand, to avoid collapsing the cavity wall, the heat should not be too much.

3.3.2 Wet-Etching

Optionally, after cleaving, the diaphragm is thinned by polishing or chemically etching (e.g., in HF) the exterior surface of the diaphragm. Etching is generally preferred over polishing, because it can provide diaphragm thickness with higher accuracy (e.g., submicron) for a controlled duration. Also, the pressure sensitivity of the diaphragm can be monitored while the diaphragm is being thinned.

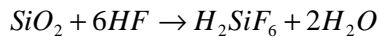
Etching can be described as pattern transfer by chemical/physical removal of a material from a substrate, often in a pattern defined by a protective mask layer (e.g., a resist or an oxide).^[17] Mask-based etching is divided into dry etching and wet etching. Wet etching is a technique that etching is in the liquid phase. Compared to the dry etching, wet chemical etching provides a higher degree of selectivity. In addition, wet etching often is faster and cheaper. In our research, wet etching method is chosen.^[18]

3.3.2.1 Rod Etching

When the diaphragm is formed by cleaving a piece of fused silica rod, the etching process is done by immersing the complete sensor into 49% HF etchant.

HF-based etchants are used mainly for silicon dioxide, because they have been observed to etch polysilicon very slowly. The most significant effects on wet-etch rates are as follows: temperature, impurities in or on the material being etched, and contamination. For fused silica, the etch rate in 49% HF at the room temperature is about 1 μm per minute.^[19]

For pure HF etching, the overall reaction is



HF is a weak acid; it does not completely dissociate into H^+ and F^- ions in water. The etch rate of silicon dioxide increases linearly with the concentrations of both HF and HF_2^- , while being independent of the concentration of F^- ions alone. The

HF_2^- complex attacks oxide about 4.5 times faster than HF. Higher-order complexes, such as H_2F_3^- , appear to occur at higher HF concentrations (e.g. 49%HF) and attack oxide even faster than HF_2^- . Thus, the etch rate increases faster than linearly with HF concentration.^[20]

So the total etch rate curves are not linear. After certain amount of time, the etch rate decreases a little. The reason is that HF molecules and HF_2^- ions are consumed with time and make the HF concentration smaller than it was at the very beginning. ^{[21] [22]}

3.3.2.2 Fiber Etching

In our experiment, the diaphragm is formed by splicing a piece of 62.5/125 fiber with a 105/125 optical fiber, as described in 3.2.2.2. In this case, fiber etching is needed to thin the diaphragm.

Optical fibers are drawn from fused silica and chemically doped to slightly change the refractive index of either the core or cladding. The 105/125 optical fiber has a fluorine-doped cladding with a smaller refractive index than that of the core. The etching rate of the core (fused silica) is about $1\mu\text{m}$ per minute. The 62.5/125 optical fiber is doped with germanium to increase the refractive index of the core. The etching rate of the core is about $24\mu\text{m}$ per minute, while the cladding (fused silica) etching rate remains $1\mu\text{m}$ per minute. The doped core is recessed by etching with an etchant that eats the core faster than the etch-resistant cladding. The depth of the recess can be controlled by the etching time. ^[23]

As discussed in 3.2.1, a cavity is formed in a hollow fiber. The inside diameter of hollow fiber, i.e. the freestanding diameter of the diaphragm, is $75\mu\text{m}$, much smaller than the core diameter of the 105/125 fiber. The 62.5/125 fiber acts as a etch barrier. A slight over-etch is required to ensure the etch reaches the barrier layer and the central portion of the cavity floor is flat. The depth of the recess determines the diaphragm thickness. A diaphragm can be controlled in the scale of sub-microns.

Chapter 4 Laboratory Test Result

After the sensors were fabricated, they were tested to evaluate their performance and calibrated for future measurement applications. We first conducted testing and calibration experiments in the lab, which is the focus of this chapter. Then the sensor was field tested in a jet engine and results are given in the next chapter.

In this chapter, the laboratory testing procedures and results are presented in detail. After the testing system is introduced, the algorithm to calculate the airgap change is given. Different algorithms are utilized based on the spectrum. Then the sensor's performance, including results from the static and dynamic pressure test, are discussed. Finally, a model to estimate the loss is presented.

For a pressure sensor, the following parameters are of main interest.

- ◆ Static pressure
 - Sensitivity
 - Repeatability
 - Hysteresis
 - Temperature dependence

- ◆ Dynamic pressure
 - Frequency response

We will discuss sensors' performance in detail in the following paragraphs.

4.1 Static Pressure Test

4.1.1 Testing System Setup

Figure 4-1 illustrates a static pressure measurement method. The sensor is sealed in a pressure chamber where the pressure is supplied by a gas system and controlled by a Pressure Systems, Inc. (PSI) pressure controller. The sensor output was detected using the CTS, as presented in Chapter 2. The reflected signal data is collected by a computer. The cavity length was determined through the interference pattern. The sensor testing system was constructed based on a computer-controlled pressure generator/controller manufactured by Pressure Systems, Inc. (PSI). The pressure controller/generator can supply a static pressure up to 200psi, and the accuracy of the pressure output is 0.1% of the full scale. The system allows us to test many

performance characteristics of the pressure sensor, such as sensitivity, repeatability, hysteresis and temperature dependence.

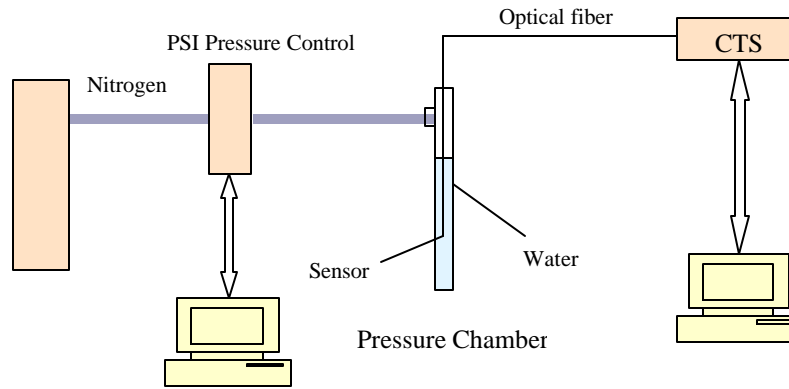


Figure 4-1 System testing setup

4.1.2 Algorithm

Various methods have been developed to demodulate the air gap from the normalized interference spectrum. In this section, two different data processing methods, including a two peak algorithm and a one peak algorithm, are described in detail. ^[24]

4.1.2.1 Two Peak Algorithm

Using two or more special points, such as peak and valley points in the interference spectrum, it is easy to acquire the absolute value of air gap. Figure 4-2 shows the spectrum of a $42\mu\text{m}$ cavity sensor. The x-axis indicates the wavelength in μm . The y-axis indicates the corresponding signal strength in dB. The CTS sweeps and shows the signals in the wavelength range between 1520 and $1570\mu\text{m}$. In the case of a $42\mu\text{m}$ cavity sensor, two valleys are observed within this range. According to the interference theory, the peak position shows that the two beams constructively interfere, and the signal reaches its maximum when the phase difference is an integral multiple of 2π . Because the second beam is reflected from the interface between the air and the fused-silica fiber, the phase will encounter a half-wavelength loss.

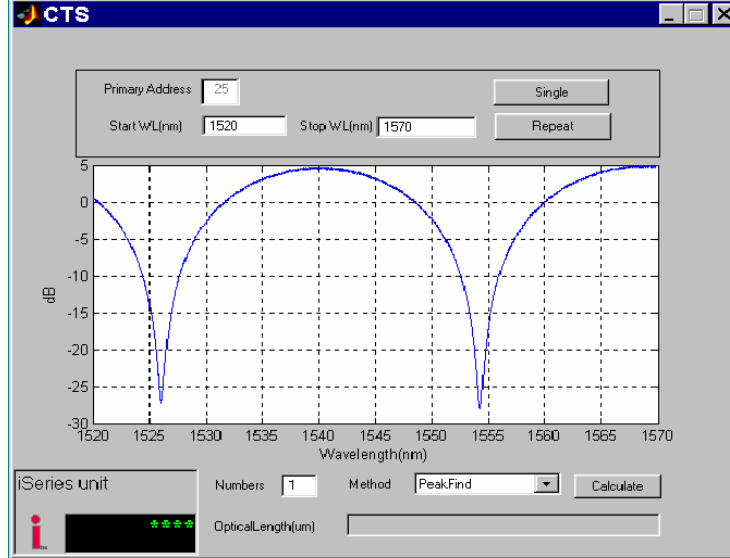


Figure 4-2 a 42μm cavity sensor spectrum in CTS

Here, the valleys are used to calculate the airgap. According to equation (2-26),

$$I_r = I_1 + I_2 + 2\sqrt{I_1 I_2} \cos\left(\frac{4pd}{l} + j_0\right) \quad (4-1)$$

$$\frac{4pd}{l_1} + j_0 = 2mp \quad (4-2)$$

$$\frac{4pd}{l_2} + j_0 = 2(m+1)p \quad (4-3)$$

m is an integer, d is the airgap. By subtracting these two equations, the airgap can be calculated by the following equation.

$$d = \frac{l_1 l_2}{2(l_1 - l_2)} \quad (4-4)$$

Obviously, this method overcomes the ambiguity problem. Yet the resolution of this method is low:

$$\left| \frac{\Delta d}{d} \right| \approx \left| \frac{l_2}{l_1 - l_2} \right| \left| \frac{\Delta l_1}{l_1} \right| \quad (4-5)$$

When pressure is applied to the sensor, the airgap will decrease because of the deflection of the diaphragm. The spectrum will shift accordingly. By taking advantage of this algorithm, the airgap change can be obtained and the pressure measured.

4.1.2.2 One Peak Algorithm

When the cavity of the sensor shrinks, only one valley can be observed in the range of 1520 and 1570 μm on the CTS, as shown in Figure 4-3. In this case, the two peak algorithm fails.

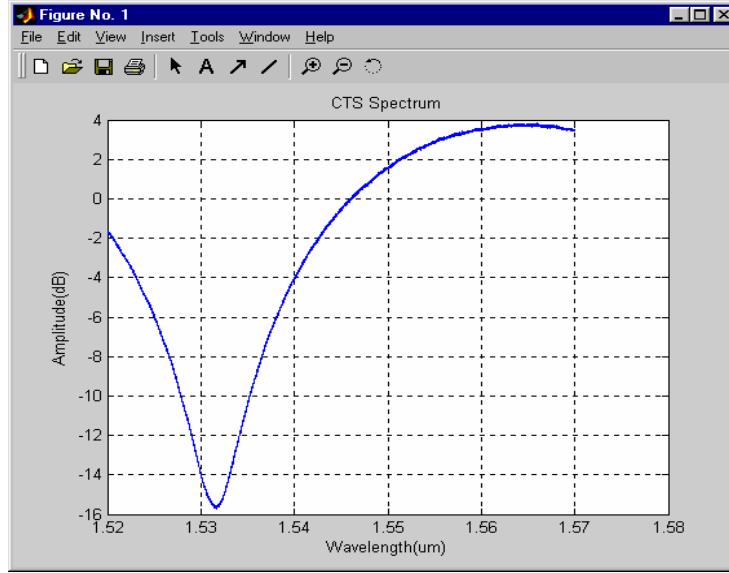


Figure 4-3 Spectrum of sensor in CTS (only one valley is observed)

Fortunately, the sensor's cavity can be estimated by using the splicer. During fabrication, the cavity length is monitored by the microscope. After fabrication, the cavity length can be estimated using the splicer LCD display. The estimation error is in the range of 3~4 μm . By inputting the estimated cavity length into the equation, the estimated m number can be obtained. Since m should be an integer, the accurate m is obtained by rounding off the estimated m number. Then, by substituting the accurate m back into the equation, the accurate cavity length can be obtained.

$$\frac{4pd}{l} + j_0 = 2mp \quad (4-6)$$

The resolution of this algorithm is

$$\left| \frac{\Delta d}{d} \right| \approx \left| \frac{\Delta I}{I} \right| \quad (4-7)$$

This algorithm neglects the initial phase, and the rounding process could induce a measurement error of half the optical wavelength. (In our case, the wavelength is 1550nm, so the maximum error is about 775nm.)

Fortunately, our goal is to acquire the pressure value by the relative airgap change. The wavelength shift of one fringe peak is employed to detect the small cavity length perturbations induced by the applied pressure, so the absolute airgap value is less

meaningful to our application. Also, the phase change caused by the airgap change is smaller than 2π . So this method is appropriate and sufficient for our test.

Normally, the spectral resolution, a parameter used to describe the ability of a spectrometer to separate two closely spaced peaks in a spectrum, is very important in spectroscopic applications. In our case, to resolve the peak position accurately, the critical factors are stability, the number of pixels in the CCD detector, and the signal-to-noise ratio. To improve the signal-to-noise ratio, a smoothing digital filter is used as the first data processing step. Then the rough peak position is found by searching the local maximum in the spectrum. In the final step, all the pixels within a suitable range from the rough peak will be used to calculate the accurate peak position. Using this method, the peak position can be determined very accurately even with a low-cost spectrometer.

4.1.3 Performance

The sensor's performance, including sensitivity, repeatability, hysteresis and temperature dependence, was tested and is presented in the following paragraphs.

4.1.3.1 Sensitivity

Figure 44 shows the sensor response to a pressure change of 10 psi. The pressure range is between 20psi and 30psi; the interval is 1psi. The pressure was first increased and then decreased to test for hysteresis. The same procedure was repeated three times to test for repeatability. After changing the pressure, it was maintained for 1 minute to allow the sensor to stabilize. By averaging all the data during that time, we obtain a point corresponding to a given pressure. The relationship between the airgap and the applied pressure can be determined by fitting a line to these points.

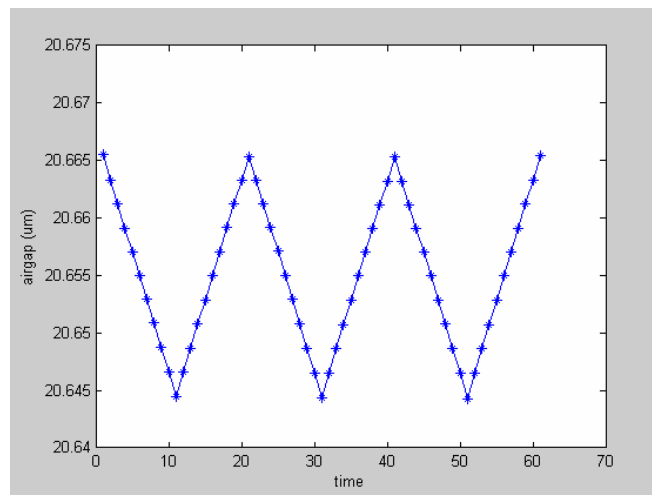


Figure 4-4 Sensor airgap change according to 10psi pressure variation

According to the definition of sensitivity, the actual sensitivity of the sensor is: $\frac{20.666 - 20.644}{10} = \frac{0.022}{10} = 0.0022(\text{nm} / \text{psi}) = 2.2(\text{nm} / \text{psi})$. The sensitivity is high enough for both medical pressure application and engine dynamic pressure test, and can be further improved by thinning the diaphragm.

4.1.3.2 Resolution

The CTS's range is $1570 - 1520 = 50(\text{nm})$, with 20,000 pixels. So the resolution is

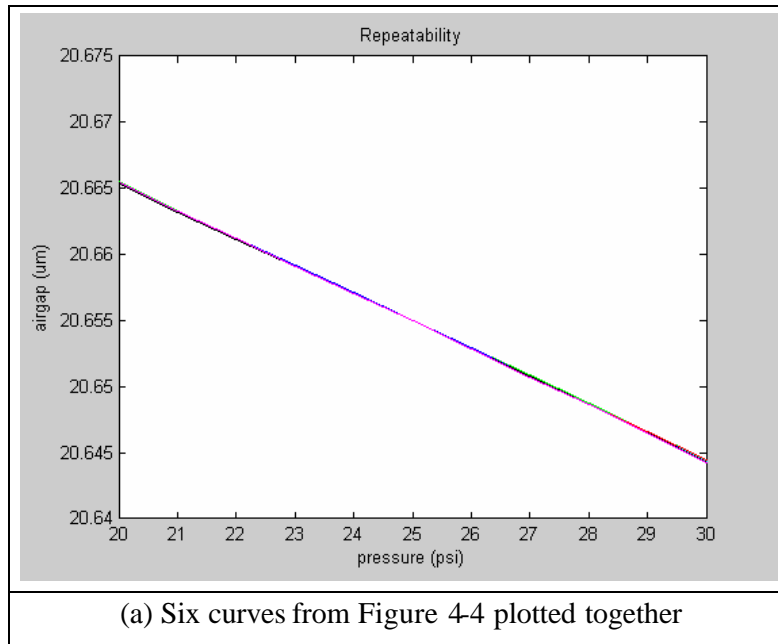
$\frac{50}{20000} = 2.5(\text{pm})$. Accordingly, the resolution of this sensor with sensitivity of

$2.2\text{nm}/\text{psi}$, is $\frac{2.5 \text{ pm}}{2.2 \text{ nm} / \text{psi}} = 1e-3 \text{ psi}$. When the full range of the measured pressure is

10psi , the resolution is $\frac{1e-3 \text{ psi}}{10 \text{ psi}} \times 100\% = 0.01\%$.

4.1.3.3 Repeatability and Hysteresis

To test the repeatability of the sensor, all six curves in Figure 4-4 are plotted together with different colors, as shown in Figure 4-5. Enlargement of the area of maximum hysteresis is shown in Figure 4-5 (b). The x-axis is the applied pressure in psi. The y-axis is the airgap in μm . Green, red, blue, cyan, black and magenta represents the 6 curves while the pressure is increasing and decreasing in the time sequence.



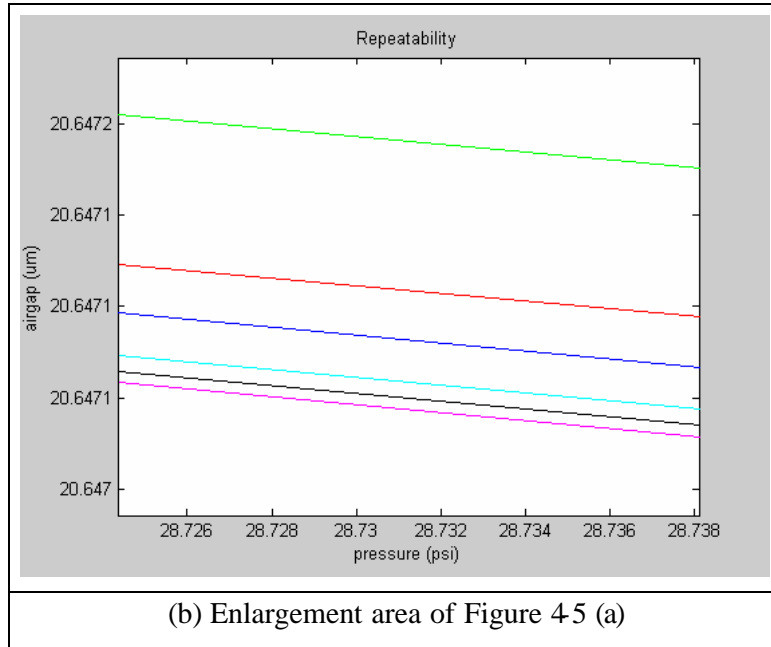


Figure 4-5 Sensor's repeatability and hysteresis

The difference between outputs for a given pressure value under rising and falling heads is termed hysteresis. The mechanism which induces hysteresis is energy absorption in the elastic member produced by molecular friction and appears as heat in dynamic cycling. It is due to the homogeneous displacement of all the atoms in the crystal lattice from their equilibrium positions. ^[24] The sensor probe is made of silica glass material and the operating range of the sensor in terms of pressure induced strain is very small. Therefore, the hysteresis of the sensor is expected to be small.

The numerical value of hysteresis can be specified by specifying the difference between the ascending and descending values, usually at midscale, as a percentage of full scale.

$$\text{Round 1: } \frac{20.64721 - 20.64715}{20.665 - 20.645} \times 100\% = 0.3\% \quad (4-8)$$

$$\text{Round 2: } \frac{20.64713 - 20.647115}{20.665 - 20.645} \times 100\% = 0.075\% \quad (4-9)$$

$$\text{Round 3: } \frac{0.000005}{0.02} \times 100\% = 0.025\% \quad (4-10)$$

The hysteresis decreases with subsequent pressure cycles. This may be caused by residual stress inside the sensor material. During fabrication, the temperature is increased and cooled down in a short period of time; the outer portion of the material can stretch and compress during this time, while the inner portion does not have time to finish its deflection. This induces stresses between the molecules. When pressure is applied, this residual stress tends to be released. This effect causes hysteresis.

Residual stresses originally present will change and generally level off or fade under repeated stressing. This “stress cycling” of parts and temperature “stress relief” will reduce or eliminate residual stresses.

From Figure 4-5 (b), we can also observe that the airgap change decreases under the same applied pressure if the sensor is repeatedly pressurized because repeated stressing can greatly reduce the residual stresses. So in order to improve sensors’ performance, we can cycle the pressure for a few rounds before calibration.

Stresses within microstructures are primarily temperature-rate-dependent. Fast cooling causes the outside part to transform to a hard structure before the inside part has a chance to cool down. When it reaches a certain temperature, it will expand against an already hardened layer, and residual stresses, distortion, and possibly even cracking will be produced.

Under natural conditions, the surface of molten glass will cool more rapidly than the centre. This results in internal stresses which may cause the glass sheet or object to crack, shatter or even explode some time later. The annealing process is designed to eliminate or limit such stresses by subjecting the glass to strictly controlled cooling in a special oven known as a "lehr". Inside the lehr, the glass is allowed to cool to a temperature known as the "annealing point". When the glass reaches this point, the lehr temperature is stabilized for a specific length of time (depending on the glass type, its thickness, its coefficient of expansion and the amount of residual stress required) to allow stresses present in the glass to relax. This phase is followed by a period of cooling with a pre-defined temperature gradient.^[25]

4.1.3.4 Temperature Dependence

For a pressure sensor, the temperature effect should be as small as possible. Because this type of sensor has the potential to operate at high temperature, the temperature dependence becomes a more important issue.

The sensor was tested by placing it in a furnace. It was heated from 100°C to 600°C and maintained at 600°C for a few minutes. Then it was cooled down from 600°C to room temperature. The airgap change due to the temperature difference is shown in Figure 4-6. We compared this output with the result from the pressure measurement. In this case, the cavity length is about 33µm:

$$\text{TemperatureDependence} = \frac{32.610 - 32.585}{500} = 0.05(\text{nm}/^\circ\text{C}) \quad (4-11)$$

$$\text{Pressure Sensitivity} = 1\text{nm}/\text{psi} \quad (4-12)$$

We found that a 1°C temperature change has the same effect as 0.05psi pressure change.

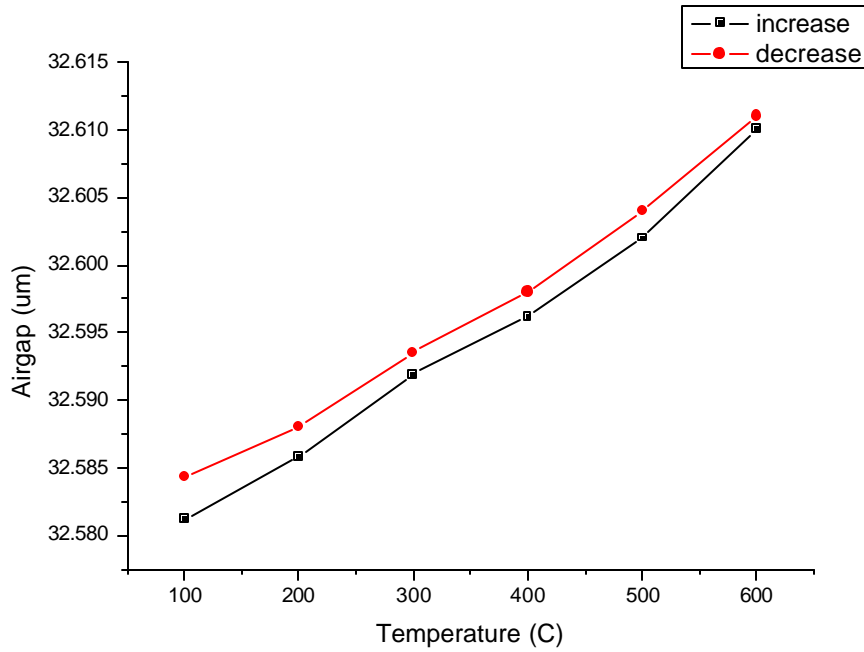


Figure 4-6 Temperature dependence of the sensor

To further analyze the underlying reasons for this temperature dependence, two main factors are considered:

For one thing, thermal expansion of the material, fused silica, causes the sensor's temperature dependence. In this case, the coefficient of thermal expansion of fused silica is $5.5 \times 10^{-7} (m/m \cdot ^\circ C)$, and this sensor's cavity length is $33 \mu m$, so the temperature effect due to this factor is calculated as:

$$\begin{aligned}
 & CTE_{silica} \times d \\
 &= 5.5 \times 10^{-7} \times 33 \times 10^{-6} \\
 &= 0.018 (nm / ^\circ C)
 \end{aligned} \tag{4-13}$$

Secondly, the air trapped inside the cavity during fabrication expands when the temperature is increased. According to the ideal gas equation:

$$PV = nRT = \text{const} \tag{4-14}$$

A very common situation is that P, V and T are changing for a fixed quantity of gas. Under this situation, (PV/T) is a constant, thus we can compare the system before and after the changes in P, V and/or T:

$$\frac{P_0 V_0}{T_0} = \frac{P_1 V_1}{T_1} \tag{4-15}$$

We can consider the situation in three separate stages.

Stage 1: While the cavity is sealed by splicing the diaphragm, the temperature is increased from 25°C to 1700°C (estimated from the splicer's specifications). During this period, the sensor is not yet sealed, and equation (4-14) is not applicable. However, for approximation, it is safe enough to apply this equation in this case. Since the cavity is connected to the air pressure, P is constant. The air volume should expand from V_0 to V_1 .

$$\frac{V_0}{273 + 25} = \frac{V_1}{273 + 1700} \quad (4-16)$$

$$V_1 = 6.62V_0 \quad (4-17)$$

In this open structure, the air escapes from the cavity into the space. In other words, the air left inside the sensor, *i.e.* the pressure inside the cavity when it is completely sealed is:

$$P_1 = \frac{P_0}{6.62} \approx 0.151P_0 \approx 0.151 \times 14.7 \approx 2.22 \text{ (psi)} \quad (4-18)$$

Stage 2: After the sensor is fabricated, it suffers from temperature variation. In this condition, the sensor is sealed and the air volume inside cannot change. The pressure is calculated as:

$$\frac{P_1}{T_1} = \frac{P_2}{T_2} \quad (4-19)$$

For example, when the temperature is increased by 100°C,

$$\frac{2.22}{273 + 25} = \frac{P_2}{273 + 100} \quad (4-20)$$

$$P_2 \approx 2.96 \text{ (psi)} \quad (4-21)$$

So, the pressure difference is $\Delta P = P_2 - P_1 \approx 0.74 \text{ (psi)}$,

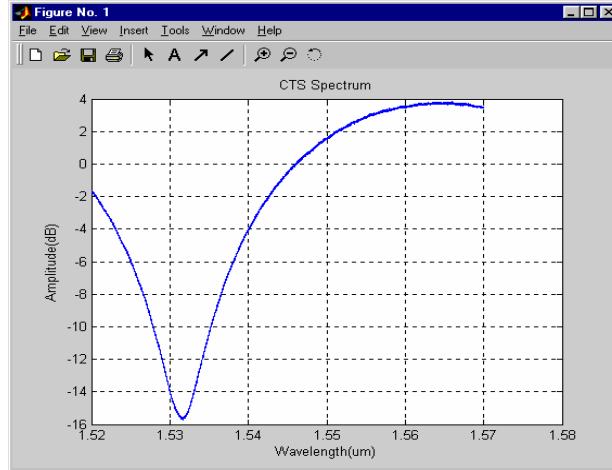
This sensor's sensitivity is about 1 nm/psi . The thermal expansion coefficient due to the trapped air is calculated as:

$$\begin{aligned} TEC &= \text{sensitivity} \times \frac{\Delta P}{\Delta T} \\ &\approx 1 \times \frac{0.74}{100} \approx 0.0074 \text{ (nm/}^\circ\text{C)} \end{aligned} \quad (4-22)$$

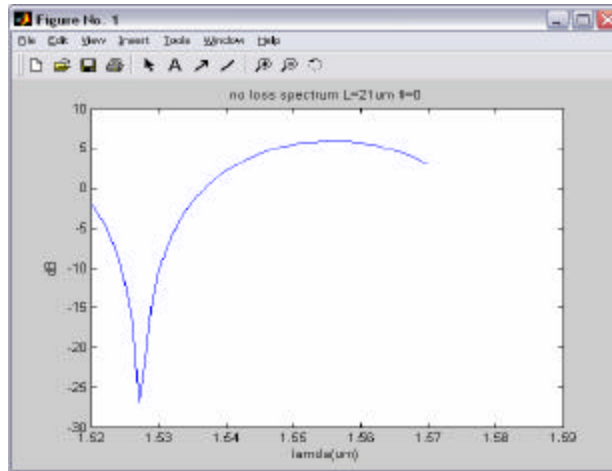
This calculation is not exactly equal to the experimental result. This may be caused by the rough estimation temperature of the splicer and the CTE of the material.

4.1.4 Loss Analysis

Light transmission losses are unavoidable. Let's compare the two plots in Figure 47. On the left is the spectrum of a real sensor whose cavity length is $21\mu\text{m}$, obtained from the CTS. The right plot is a computer simulation result. In this case, no loss is considered. So it is an ideal spectrum for the same length sensor.



(a) Experimental spectrum of the actual sensor



(b) Simulation result of spectrum of the real sensor

Figure 4-7 Comparison of the spectrum of the real sensor and the simulation result

First of all, the greatest difference is the phase shift between these two plots. The reason resides in the zero initial phase set in the ideal simulation, while this is not true in the practical case. What's more, in the ideal plot the peak can exceed 5 dB and the valley can be as low as -27 dB. The actual sensor's spectrum shows the peak no higher than 4dB and the valley no lower than -16 dB. The visibility of the sensor is reduced for many reasons. The light transmission loss is one of them.

During fabrication of the sensor, different kinds of losses can be induced. Alignment loss is due to lateral, longitudinal and angular offset. Lateral offset is the largest cause of insertion loss. One of the main factors is the loss caused by the light transmission inside the cavity, which can be regarded as longitudinal misalignment of two fibers. The loss, or equivalently the coupling efficiency between the fibers, is formally expressed in terms of an overlap integral in which the field emitted from a sending fiber is multiplied by that of a receiving fiber and is integrated over the entire cross section of the second fiber.

4.1.4.1 Gaussian Model

The transverse field distribution of the fundamental mode in a fiber can be well approximated by a Gaussian profile with an appropriate half-width parameter.^[10] With this approximation, the overlap integral mentioned above is reduced to an integral of two Gaussian fields.^[26]

The excitation of the fundamental mode in the fiber was calculated when a Gaussian beam whose waist coincides with the fiber end face is launched axially into the fiber. By selecting the spot size of the incident beam appropriately, the excitation efficiency of the mode can be maximized, and a Gaussian field having this spot size as a half-width is a good approximation to the field of the mode, since the efficiency is close to 100%. The half-width of the Gaussian profile was determined from the requirement that a Gaussian field should approximately satisfy the wave equation.

Light transmission losses of single-mode fiber depend on the alignment accuracy of the fiber ends relative to each other. The fields of single-mode fibers are very nearly Gaussian in shape. The evaluation of losses is reduced to the computation of transmission losses between misaligned Gaussian beams. The transmission coefficient of weakly guiding fiber modes can be obtained by matching only the transverse components of the electric field vector of the two modes; their transverse magnetic field components are automatically matched approximately. The incident electric field at the input end of the fiber can be expressed as the summation over guided modes (only one in SMF) and integration over radiation modes. The power transmission coefficient is obtained from c_0 :

$$E = \sum_n c_n E_n \quad (4-23)$$

$$c_0 = \frac{1}{2P} \int_0^{2p} d\mathbf{f} \int_0^\infty (E \times H_0)_z e_z r dr \quad (4-24)$$

$$T = |c_0|^2 \quad (4-25)$$

T : transmission coefficient

According to the empirical formula,

$$\frac{w}{a} = 0.65 + \frac{1.619}{V^{\frac{3}{2}}} + \frac{2.879}{V^6} \text{ for step index fibers;} \quad (4-26)$$

$$\frac{w}{a} = \sqrt{\frac{2}{V}} + \frac{0.23}{V^{\frac{3}{2}}} + \frac{18.01}{V^6} \text{ for parabolic-index fiber.} \quad (4-27)$$

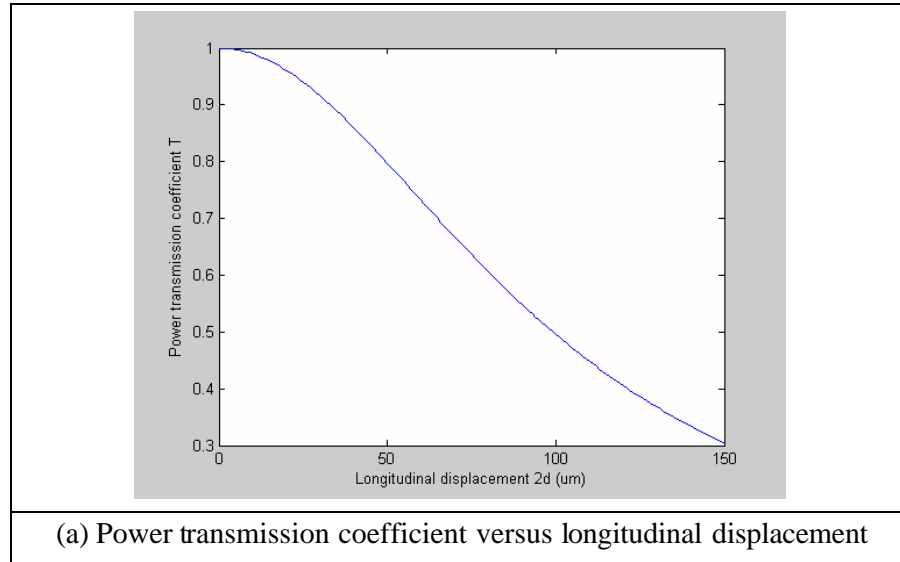
w : optimum width of the Gaussian field profile
 a : core

For longitudinal separation,

$$T = \frac{4 \left[4Z^2 + \frac{w_1^2}{w_2^2} \right]}{\left[4Z^2 + \frac{w_2^2 + w_1^2}{w_2^2} \right]^2 + 4Z^2 \frac{w_2^2}{w_1^2}} \quad (4-28)$$

$$Z = \frac{L}{n_2 k w_1 w_2} \quad (4-29)$$

Figure 4-8 shows the simulation results according to the previous discussion. Similarly, there are relationships between both the tilt angle and the amount of offset and the power transmission coefficient. Loss can thus be estimated from this analysis.



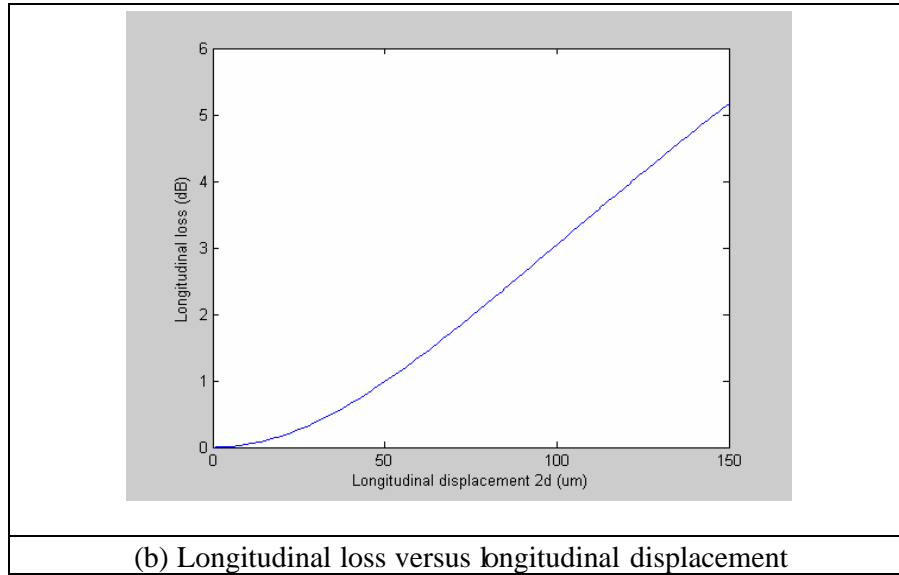


Figure 48 Matlab simulation of the relation between power transmission coefficient (a) and longitudinal loss (b) with the longitudinal displacement

4.1.4.2 Longitudinal Loss

Another way to estimate the longitudinal loss is the geometrical method. It is simpler and sufficient for understanding the drop in the output intensity of the sensor as a function of the gap displacement. Figure 49 illustrates the sensor's structure, and Figure 4-10 shows the field size that can be calculated by the geometrical method.

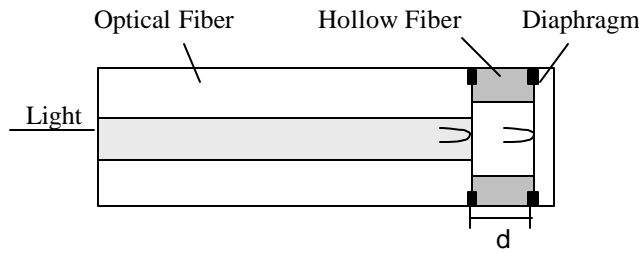


Figure 4-9 Sensor structure

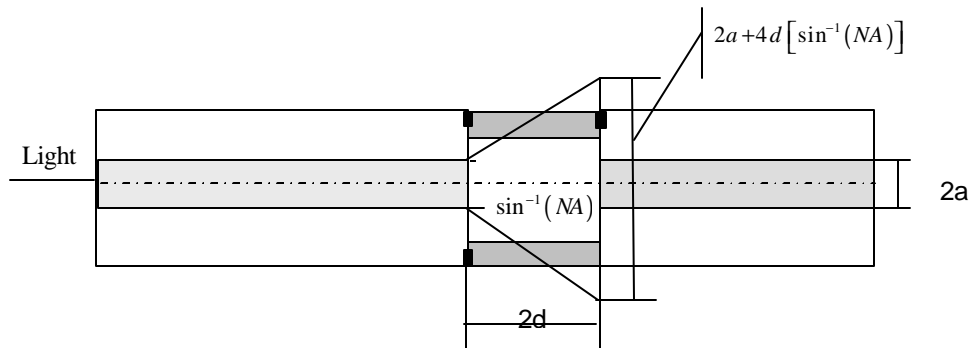


Figure 4-10 Geometrical analysis of the longitudinal loss

$$A_2 = A_1 \times \left\{ \frac{ta}{a + 2d \tan \left[\sin^{-1}(NA) \right]} \right\} \quad (4-30)$$

A_1 : the reference reflection coefficient

A_2 : the sensing reflection coefficient

t : transmission coefficient of the air-glass interface

a : fiber core radius

d : cavity length

NA : numerical aperture

Accordingly, the transmission coefficient and transmission loss can be calculated with the similar algorithm presented above.

4.2 Dynamic Pressure Test

4.2.1 Testing System Setup

Figure 4-11 illustrates the experimental setup for dynamic pressure measurements. The sensor is mounted directly facing the transducer driven by a signal generator and the amplifier. The working frequency of the transducer is 45 kHz. Its -6dB bandwidth is 6.0 kHz. And the sound pressure level is about 110dB at 1 meter. The source acoustic signal is investigated by an oscilloscope. The sensor output data is collected and analyzed by photodetector and another oscilloscope.

The detection part of the configuration is similar to that of the static pressure test setup. In order to increase the signal to noise ratio, the working point is tuned to its Q-point. This is realized by a tunable filter which can run through more than one fringe of the sensor's output. The pictures of the equipment are shown in Figure 4.12.

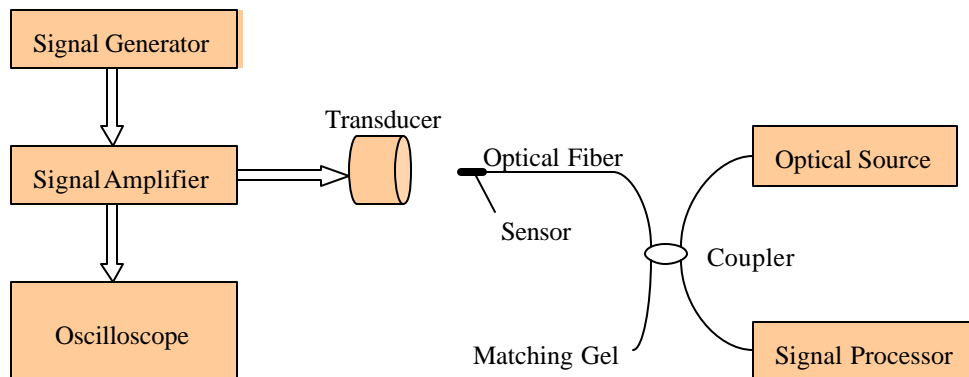


Figure 4.11 Experimental setup for dynamic pressure test

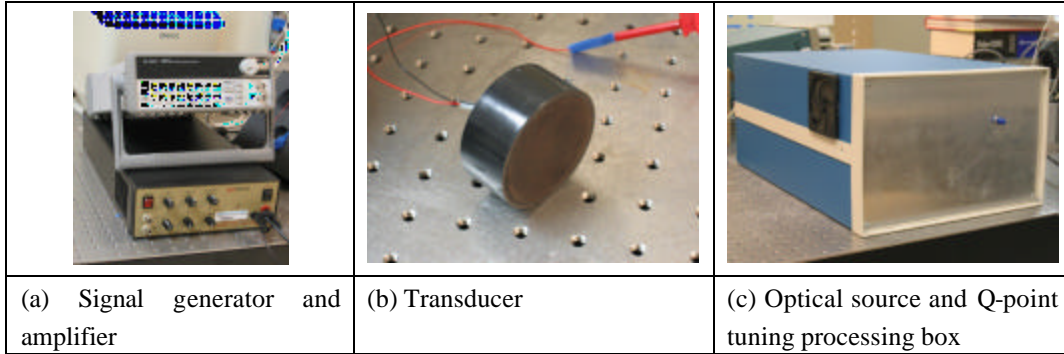


Figure 4-12 Pictures of the equipment for the dynamic pressure test

4.2.2 Frequency Response

The pressure sensor generally has a very high resonant frequency as a result of its small size. Hence, the sensor is well suited for measuring rapidly changing dynamic pressures. Also, the sensor tends to have a highly linear response and very low hysteresis. Figure 4-13 illustrates the oscilloscope output. The yellow signal indicates the time-domain signal, while the red one is the FFT of the time-domain signal. Clearly, a high peak at 46.9kHz can be observed, which means that the sensor is capable of detecting the acoustic signal from the 46.9kHz source. Figure 4-14 shows the FFT result of the time-domain signal. Matlab was utilized to analyze the data and plot the figure. In the field test described in the following chapter, we will take advantage of the program to analyze the data.

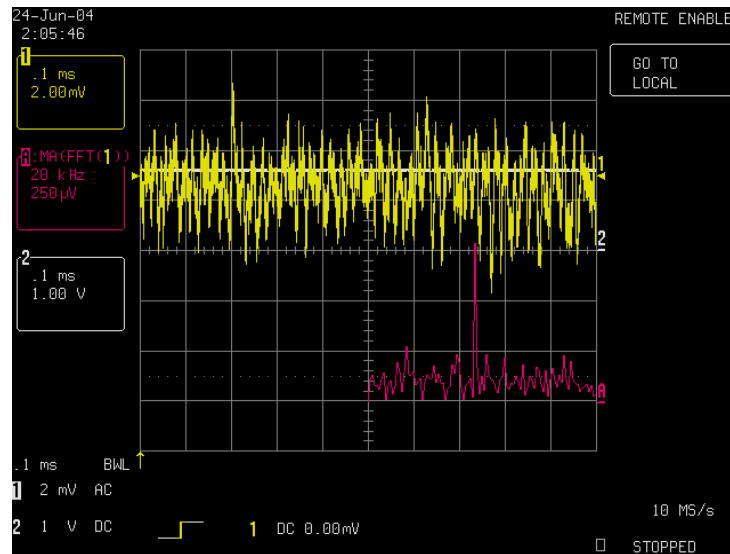


Figure 4-13 Signal output from the oscilloscope during the dynamic pressure test. Time-domain signal (yellow) and corresponding FFT (red).

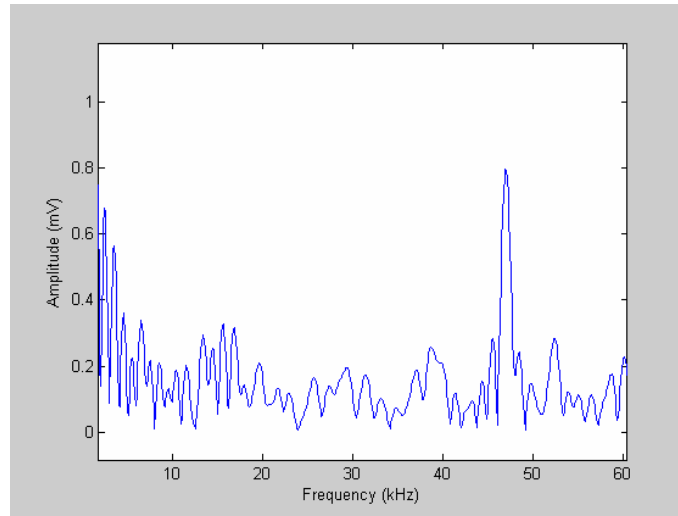


Figure 4-14 FFT of the time-domain data as analyzed by Matlab.

4.3 Dynamic Pressure Calibration

Dynamic pressure calibration is more challenging and less accurate than static pressure calibration. Dynamic calibration is generally accomplished by venting the sensor being calibrated to a known static reference pressure by means of a fast-acting valve^[27], but no such devices are available in our lab.

However, since the operating frequency is far below the natural frequency, the sensor can be roughly calibrated by its static pressure.

According to (2-34), its resonant frequency is obtained by:

$$f_{00} = 2.749 \times 10^9 \times \frac{h}{r^2} \quad (4-31)$$

Generally, the sensor's thickness is $2.5 \mu\text{m}$, its freestanding radius is $75/2 = 37.5 \mu\text{m}$. By inputting this coefficient into (4-31), we can see that the resonant frequency is about 9.7 MHz. Since the sensor works at 10 – 60 kHz, which is much lower than its resonant frequency, we can consider the sensor's frequency response to be very flat in the low frequency range. Under this assumption, the sensor's response at such low working frequency is presumed to be the same as that at room pressure. As a consequence, we use the slow static pressure change result to calibrate the sensor. A typical response is about 15.7 mV/psi. In order to further testify the performance of the optical sensor, a commercial Kulite sensor was utilized for reference. The Kulite sensor's response is about 33 mV/psi.

Chapter 5 Engine Field Test Result

On June 24th, 2004, we successfully installed and tested the miniature fiber tip pressure sensor near the fan of a turbo engine. This chapter shows the installation location of the sensor in the engine; presents the packaging of the optical fiber sensor; and analyzes the performance of the optical sensor compared with that of the commercial Kulite sensor. Results from both sensors show that the acoustic pressure around the fan of the engine is about 0.89psi. Also, the phase delay between the optical sensor and the Kulite sensor coincide with the calculated value based on the distance between these two sensors. The entire test procedure proves that the sensors' package and installation are safe for the engine operation and the sensors' performance is good near the fan.

5.1 Installation Location in the Engine

The installation location of the sensors is shown in Figure 5-1 (a) shows the five holes in the ring encircling the fan of the engine which are used for sensors installation. (b) illustrates the enlarged picture of the installation location from the inside view. (c) shows an enlarged external view of the installed sensors. The center hole is for the installation of the commercial Kulite sensor which served as a reference during our test. The miniature fiber tip sensor is positioned 40mm away from the Kulite sensor, as shown in (c).

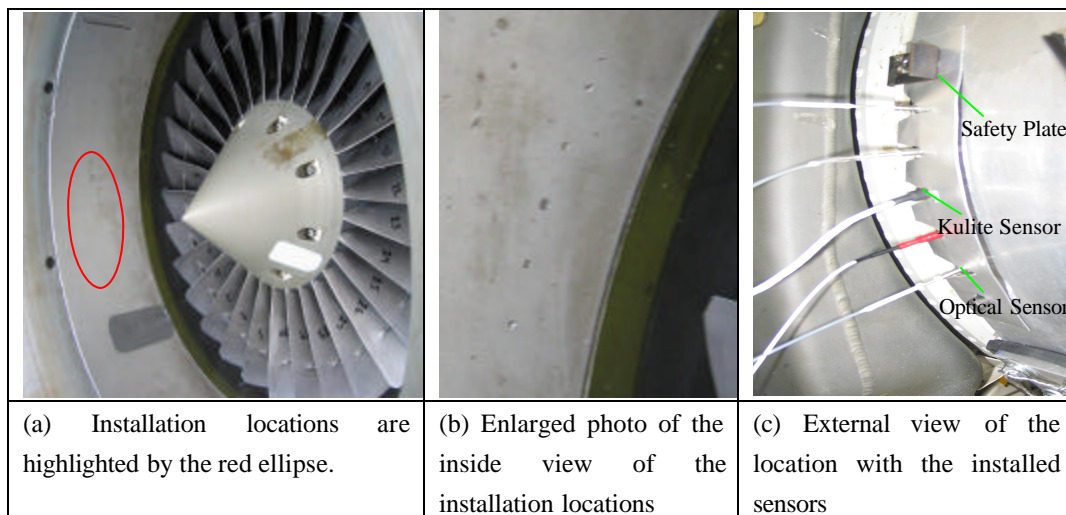


Figure 5-1 Installation locations of the sensors during the engine field test.

5.2 Package Description

The package of the optical fiber tip pressure sensor was carefully designed to satisfy safety considerations. The details of the configuration shown in Figure 5-2 and the size of different parts are illustrated in Figure 5-3 and Figure 5-4.



Figure 5-2 Picture of the packaged sensor

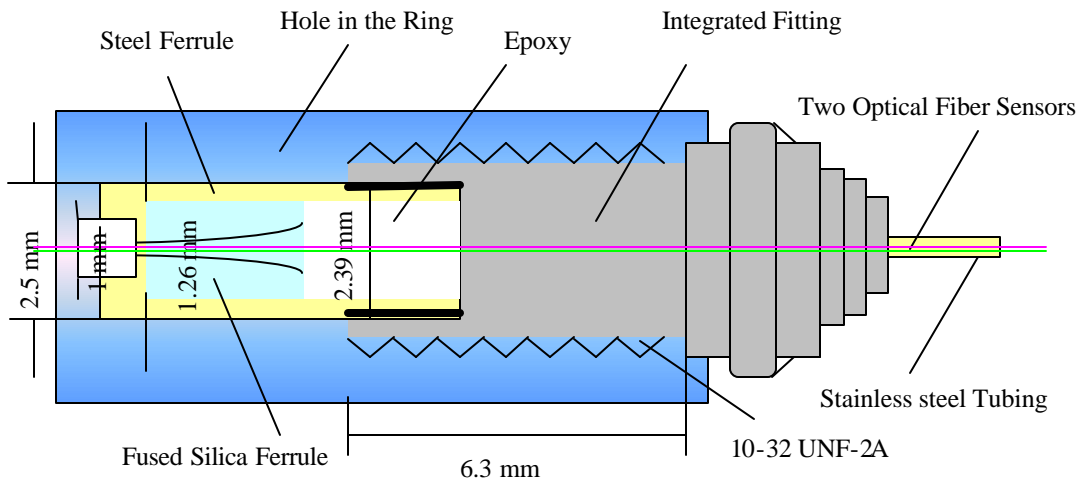
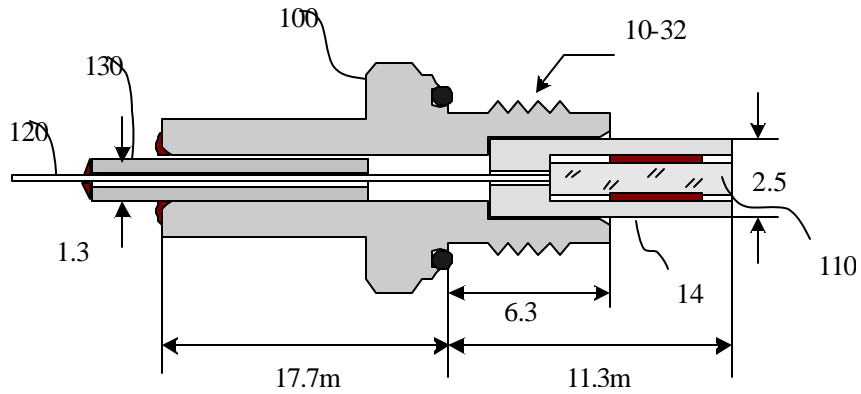


Figure 5-3 Schematic of the optical sensor packaging configuration (not to the scale).



- 100: Stainless steel fitting
- 110: Fused silica ferrule
- 120: Optical fiber
- 130: Stainless steel tubing
- 140: Steel Ferrule

Figure 5-4 Cutaway view of the fiber optic pressure sensor packaging

Two optical fiber sensors whose diameters are $125\mu\text{m}$ at the sensing head and $250\mu\text{m}$ in the remaining parts are inserted into a fused silica ferrule (110), which is embedded in a steel ferrule (140) with a concave aperture. This design prevents the fused silica ferrule from being sucked into the engine during operation. The steel ferrule (140) is then fixed to the standard integrated steel fitting (100) by epoxy. At the other end of the sensor, the optical fiber is protected by a piece of stainless steel tubing (130) which is bonded to the fitting (100) with epoxy.

During the field test, the whole packaged optical sensor was screwed into the prepared hole in the ring around the fans of the engine. For safety reasons, the holes are non-flush with concave orifice in order to avoid the whole packaged sensor falling into the engine. In addition, as shown in Figure 51(c), in case the vibration of the engine loosens the screwed packaged sensor and sucks the elements inside, an aluminum safety plate with an orifice size smaller than the sensor is fastened by two long screws at the back of the sensors.

5.3 Performance Analysis

Before the field test, the optical sensors were calibrated. Their response was about 15.7mV/psi . In order to further confirm the performance of the optical sensor, a commercial Kulite sensor was utilized for reference. The Kulite sensor's response was about 33mV/psi . Figure 5-5 and Figure 5-6 show the frequency and time domain signal response to the acoustic pressure near the engine fan when the engine was running at about 90% of its full speed.

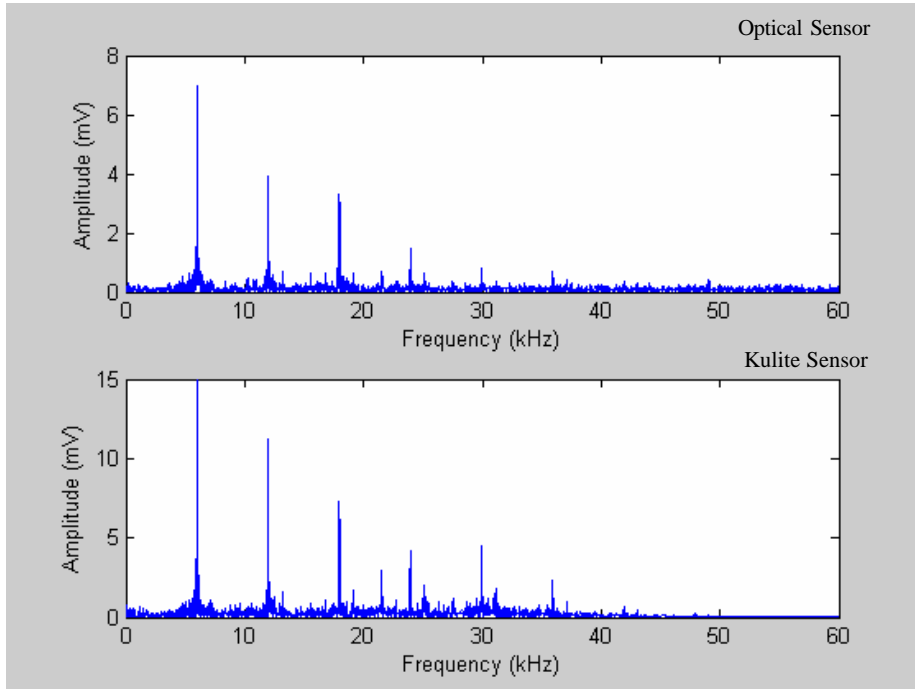


Figure 55 Frequency response of the optical sensor compared with that of the Kulite sensor. (The top plot shows the response of the optical sensor while the lower one shows the response of the Kulite sensor.)

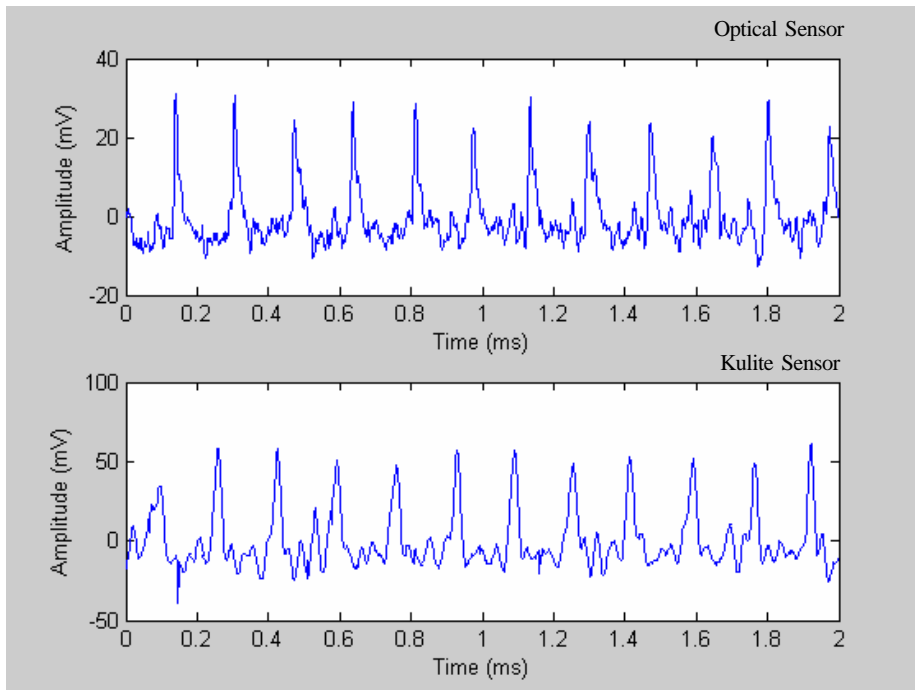


Figure 56 Time domain response of the optical sensor compared with that of the Kulite sensor. (The top plot shows the response of the optical sensor while the lower one shows the response of the Kulite sensor.)

Figure 5-5 shows that both the optical sensor and the Kulite sensor have a high response to the fundamental frequency and its multiple frequencies. Here the analysis and comparison of the responses are given up to sixfold frequency. Their frequency and corresponding signal amplitude are listed in Table 5.3.1-1.

Table 5-1 Comparative results between the optical sensor and the Kulite sensor.

	Frequency (kHz)		Amplitude (mV)	
	Optical Sensor	Kulite Sensor	Optical Sensor	Kulite Sensor
Frequency 1	5.985	5.985	7.0198	14.8556
Frequency 2	11.970	11.970	3.9559	11.1985
Frequency 3	17.960	17.955	3.3262	7.2848
Frequency 4	23.945	23.940	1.4419	4.1817
Frequency 5	29.940	29.930	0.8255	4.5464
Frequency 6	35.923	35.915	0.6702	2.3301

Table 5-1 shows little difference between the results of the fundamental frequency and its multiple frequencies obtained from these two kinds of sensors. This consistency between the optical sensor and the commercial Kulite sensor is a strong support for the validity of the optical sensor.

5.3.1 Acoustic Pressure Measurement Result

First, the Kulite sensor's measurement result is analyzed. As given in the description, its response is about 33.3mV/psi. The field test results given by Table 5-1 show that for the fundamental frequency, the sensor's response is 14.8556mV. The peak to peak value is $14.8556 \times 2 = 29.7112$ (mV). The acoustic pressure around the fan of the engine is: $29.7112/33.3 \sim 0.8922$ (psi).

Then, the optical sensor's result is given. Laboratory calibration results show that this sensor's response is about 15.7mV/psi. The field test result shows that for the fundamental frequency, the sensor's response is 7.0198mV. The peak to peak value is $7.0198 \times 2 = 14.0396$ (mV). So the acoustic pressure around the fan of the engine is: $14.0396/15.7 \sim 0.8942$ (psi).

Except for the slight discrepancy which may be caused by calibration error, the above calculation shows that two results coincide with each other. This further proves that the optical sensor functions well during the engine pressure test.

5.3.2 Time Delay Analysis

Figure 5-2 shows the time domain signal from the optical sensor and the Kulite sensor. A constant phase delay (time delay) is obvious. This is caused by the distance between the installation positions of the optical sensor and that of the Kulite sensor. Estimation of the phase delay can be done by the following calculation.

The distance between the Kulite sensor and the optical sensor is 40mm. The radius of the ring surrounding the fans is 254mm. Rotation speed of the fan is about 200 rounds/second. So the time delay between the Kulite sensor and the optical sensor can be estimated as $\frac{40}{2\pi \times 254} \times \frac{1}{200} \approx 0.13 (ms)$.

Figure 5-2 shows that the time delay between the optical sensor and the Kulite sensor is about 0.12ms. The estimated result agrees well with the experiment result. The error may be caused by the rough measurement of the distance between sensor positions and the ring radius. Also, the rotation speed is not ideally constant when the engine is operated at 90% of its full speed.

5.4 Summary

The field test result confirms that the optical sensor design can function safely and reliably near the engine fan. During about two hours of field testing, the optical sensors' package is robust enough for the engine operation. In addition, the optical sensor is able to measure the acoustic pressure near the engine fan. Its performance coincides with that of the commercial Kulite sensor.

Furthermore, theoretical calculation and analysis indicate that the sensors can work well under a higher temperature and pressure environment, where most current commercial sensors cannot survive. This is to be further proven by experiments.

Chapter 6 Conclusions and Future Work

6.1 Conclusions

As presented in the previous chapters, this miniature fiber tip pressure sensor is suitable for medical diagnostics, environmental monitoring and other industrial applications. Its unique features include its micron scale size, light weight, simple structure, low cost, robust design, real-time data processing, EMI immunity, extreme high temperature and pressure endurance, and corrosion and chemical inertness.

Based on the EFPI principle, the diaphragm-based fiber tip pressure sensing technique was designed, developed and evaluated. The fabrication process is simple and includes only cleaving and splicing steps. The Fabry-Perot cavity is formed by the cleaved ends of fibers, which have ultra smooth and uniform surfaces. Cavity length can be adjusted as required. To increase the sensitivity, MEMS techniques, such as wet chemical etching, were successfully combined and used in the diaphragm fabrication process. Specifically, these techniques were implemented on the fused silica fiber to thin the diaphragms. The total time required by fabrication is generally less than an hour.

Experimental test results both in the laboratory and in the field indicate that the fiber tip sensor can fulfill the specific requirements for the engine testing. Static pressure, dynamic pressure, sensitivity, repeatability, hysteresis, and temperature dependence of the sensor were measured. In addition, field test results using the fiber tip sensor in a jet engine were analyzed and compared with a commercial Kulite sensor reference. Experimental data indicate that this type of sensor is a good candidate for high temperature (600°C) environments.

6.2 Future Work

Based on the previous work described in this thesis, there is much potential for the sensor head and testing system to be improved in the future. The parameters of basic fabrication operations, including fusion splicing, cleaving and etching, can be adjusted to improve the sensors' performance. Also, other materials and bonding methods can be adopted to satisfy different application requirements. Additional issues may also be considered to increase the sensor performance and cut down the cost. The following objectives should be pursued in the future to improve performance and to open up new application areas for such sensors.

6.2.1 Cleaver Adjustment

Currently, all cleaving operations are performed by the Fujikura CT-04B high precision fiber cleaver. The fiber position is manually adjusted without accurate control. As a result, the thickness of the cavity and diaphragm may deviate from their optimal values. To solve this problem, precision translation stages may be utilized to accurately control the fiber position during cleaving.

6.2.2 Other Materials and Structures

In our research, the hollow fiber tube, fiber and diaphragm are all made of the same material - fused silica. The fiber is preferably a conventional index-guided single mode optical fiber, but can also be a photonic-crystal fiber, a holey fiber, or a multimode fiber. The fiber can have a graded-index or step index, or any other light-guiding profile or structure. The sensor can be made of plastic or polymeric fibers. In this case, the fiber, hollow tube and diaphragm can be bonded with adhesives, with solvents, or by thermal or ultrasonic welding.

Alternatively, the diaphragm can be made of ceramic or sapphire, which will provide a higher maximum operating temperature. If sapphire fibers are used, then a chlorine-containing plasma can be used as the etchant. For example, a BCl_2/HBr inductively coupled plasma can be used to achieve a high rate of sapphire etching, with a high selectivity over photoresist. Alternatively, the diaphragm can be formed from a thin plate or wafer bonded to the hollow tube. The diaphragm can have a layered structure comprising layers of glass, silica, polymers or ceramics. These alternative structures can enhance the flexibility of the design according to specific fabrication equipments and materials available.

Also, the interior diameter of the hollow fiber, i.e., the freestanding diameter of the diaphragm, can be varied according to different requirements.

6.2.3 Other Bonding Methods

The bonds between the fiber, tube, and diaphragm can be fusion bonds made by a fusion splicer. A fusion splice bond is particularly well suited for use with fused silica, glass or sapphire components. The fusion splice bonds can be made with a conventional electric-arc fusion splicer, as described above. The fiber, tube, and diaphragm can also be bonded in other ways, for example by anodic bonding, direct bonding, hydroxide bonding, agglutinating or by conventional adhesives such as sealing glasses or epoxy. The different bonding methods, with different bonding

strength, complexity of operation and fabrication cost, can be selected for specific applications.

6.2.4 Film Deposit

To increase the amplitude of optical interference effects in the etalon, thin film coatings can be deposited (e.g., by sputtering or other processes) on the fiber endface and diaphragm to enhance reflectivity. For example, metals (e.g., gold) or dielectrics (e.g., silicon, or TiO_2) can increase the amount of reflection. Increased interference amplitude in the etalon will tend to increase resolution and accuracy. Generally, without coating, the reflection coefficient from both sides of the interference cavity is about 4%. With a proper coating, the reflectance can reach higher than 90% and the signal to noise ratio can be greatly improved.

6.2.5 Three Cavity Problem

Three reflecting surfaces are evident: the optical fiber endface and the two diaphragm surfaces. Each will send a beam of light back into the fiber, resulting in a three-beam interference pattern, which is not the case discussed in Chapter 2 for traditional EFPI sensors. Fortunately, this will only cause minor signal processing difficulties because of the large difference between cavity length and diaphragm thickness. Also, in our static pressure test, the sensor is immersed into water to reduce the reflection from the outer surface of the diaphragm. Furthermore, this reflection can be damped by an optical absorbing coating. The spectrum will be more consistent with the description of Chapter 2, and the signal processing more straight-forward.

6.2.6 Multimode Fiber Sensors

The single mode (SM) lead-in fiber can potentially be replaced by multimode (MM) fiber, which offers a number of advantages, including high source power and insensitivity to bending loss. This will have minimal impact on the sensor fabrication procedure since the remaining sensor head components will remain the same.

6.2.7 Open Cavity Structure

The etalon cavity can be hermetically sealed, or can be open to the external environment. If the cavity is sealed, it can be pressurized or evacuated to alter the measurement range or sensitivity. A sensor with a sealed cavity can measure both

static and dynamic pressure.

If the sensor is open to the environment, the pressure sensor will be responsive to only dynamic changes in pressure. The cavity can have a small orifice to provide a fluidic connection between the cavity and external environment.

6.2.8 Dynamic Pressure Calibration

Dynamic calibration of pressure transducers is more demanding and less accurate than static methods, where measurement data can be carried out to many decimal points. Dynamic calibration is generally accomplished by venting the sensor being calibrated to a known static reference pressure by means of a fast-acting valve; by hydraulic impulse comparison calibration using a transfer standard, or with a shock tube. Depending on the type of calibrator and gas medium used, rise times on the order of milliseconds or microseconds can be achieved. Sensor mounting, switching transients, and readout accuracy all enter into the equation. Digital signal processing has greatly improved the measurement accuracy as compared with earlier methods that used analog storage oscilloscopes. The ideal dynamic calibrator would be structured to generate a precisely known reference pressure that could be continuously adjusted over a wide range of amplitudes and frequencies. But no such device exists.

In our experiments, the dynamic pressure calibration is performed by the static pressure evaluation. Since the operating frequency is far below the natural frequency, this method works quite well. However, with the help of a fast-acting valve, such as a shock tube, the calibration will be more accurate. As a consequence, the testing results will be more convincing.

6.2.9 Other Issues

In addition to the issues discussed in the previous sessions, there are more that can be improved in the future. Low cost manufacture can be achieved by pipelining and batch fabrication in industry. Fibers and hollow fibers can be aligned, cleaved and spark-spliced in a pipeline. The cavity length can be adjusted more precisely with an advanced monitoring system, such as a high magnification microscope or a scanning electron microscope (SEM). Also, MEMS processes such as wet etching can be done with many preformed sensors in the same time. Furthermore, due to the trapped air inside the cavity during fabrication, zero temperature dependence was not achieved. Improvements in sensor design and fabrication process are needed to realize this goal.

On the other hand, the sensor still has a great deal of potential for further applications. Firstly, the sensors are so small that they can be employed in dense arrays to provide

high resolution 2D or 3D sensing of pressure fields, such as mechanical vibrations, acceleration or acoustic waves. Secondly, the present pressure sensor is well suited for use in chemically sensitive environments, since it can be made of only fused silica, sapphire or other relatively inert materials. For example, the present pressure sensor is biocompatible and can be used in medical and biological applications. Thirdly, the sensor can survive in a high temperature and high pressure environment. This capability opens up a broad range of applications for such sensors. For instance, the sensor can be safely installed in different locations in an engine to measure pressures.

References

- [1] Brian Culshaw, “Optical Fiber Sensor Technologies: Opportunities and – Perhaps – Pitfalls” , *Lightwave Technology, Journal of* , Volume: 22 , Issue: 1 , Jan. 2004
Pages:39 – 50.
- [2] D.A. Krohn, *Fiber Optic Sensors, fundamentals and applications*, 3rd edition
- [3] Alan D. Kersey and Anthony Dandridge, “Application of Fiber-Optic Sensors” , *Electronic Components Conference*, 1989. *Proceedings.*, 39th , 22-24 May 1989
Pages:472 – 478.
- [4] K.T.V. Grattan and B.T.Meggitt, Ed. *Optical Fiber Sensor Technology*, Boston: Kluwer Academic , 1995.
- [5] M. Madou, *Fundamentals of Microfabrication*, Boca Raton, FL: CRC Press, 1997.
- [6] Alan Rogers, “Essentials of Optoelectronics with applications” , Chapman & Hall.
- [7] K.T.V. Grattan and B.T. Meggitt, Ed., *Optical Fiber Sensor Technology*, New York: Chapman & Hall, 1995..
- [8] John Dakin and Brian Culshaw, Ed., *Optical Fiber Sensors: Principles and Components*, Boston: Artech House, 1988.
- [9] J.A. Greene and T.A. Tran, “Applications of the Extrinsic Fabry-Perot Interferometer” , *Proc. SPIE Vol. 2510 Fiber Optic and Laser Sensors XIII*, p. 165-171, Sep. 1995.
- [10] J.M. Vaughan, *The Fabry-Perot Interferometer, History, Theory, Practice and Applications*, Philadelphia: Adam Hilger, 1989.
- [11] G. Hernandez, *Fabry-Perot Interferometers*, New York: Cambridge University Press, pp. 9– 20, 1988.
- [12] Belsley, K.L., Huber, D.R. and Goodman, J., “All Passive Interferometric Fiber-Optic Pressure Sensor” , *Proceedings of the ISA (Instrument Society of America)*, Houston, TX, pp1151-1158, 1986.
- [13] Maurice Francon, *Optical interferometry*. New York: Academic Press, 1966.
- [14] S. Timoshenko, S. Woinowsky-Krieger, *Theory of Plates and Shells*, 2nd edition, New York: McGraw-Hill, 1959.
- [15] W.Soedel, *Vibrations of Shells and Plates* , New York: Marcel Dekker , 1993.
- [16] <http://www.sciner.com/Opticsland/FS.htm>
- [17] Y.Kanda, K.Matsuda, C.Murayama, and J.Sugaya, “The Mechanism of Field Assisted Silicon-Glass Bonding” , *Sensors & Actuators*, vol. A21, pp.939-943, 1990.
- [18] Xingwei Wang, Juncheng Xu, Yizheng Zhu, and Anbo Wang, “Miniature Fabry-Perot Structure” , VTIP disclosure 04.001.
- [19] Douglas J. Markos, Benjamin L. Ipson, Kevin H. Smith, Stephen M. Schultz, Richard H. Selfridge, Thomas D. Monte, Richard B. Dyott, And Gregory Miller, “Controlled core removal from a D-shaped optical fiber” , *Applied Optics*, Vol. 42, No. 36, pp. 7121-7125. December 2003.
- [20] Bratter, R.L.,” Commercial success in the MEMS marketplace” , *Optical MEMS*,

- 2000 IEEE/LEOS International Conference on, 21-24 Aug. 2000, Pages: 29 – 30.
- [21] Kirt R. Williams, Richard S. Muller, “Etch Rates for Micromachining Process”, IEEE Journal of Microelectromechanical System, Vol. 5, No.4, pp.256-269, December 1996.
- [22] A. Berthold, P.M. Sarro, M.J. Vellekoop, Two-step Glass-etching for Micro-fluidic Devices, Proceedings of the SeSens workshop, pp. 613-616, December 1, 2000.
- [23] Axel Grosse, Matthias Grewe and Henning Fouckhardt, Deep wet etching of fused silica glass for hollow capillary optical leaky waveguides in microfluidic devices, Journal of Micromechanics and Microengineering, p257-262, 2001.
- [24] G.A.C.M. Spierings, Review Wet chemical etching of silicate glasses in hydrofluoric acid based solutions, Journal of Materials Science 28, p6261-6173, 1993.
- [25] Bing Qi, Gary R. Pickrell, JunCheng Xu, Po Zhang, Yuhong Duan, Wei Peng, Zhenyu Huang, Wei Huo, Hai Xiao, Russell G. May, and Anbo Wang, “Novel data processing techniques for dispersive white light interferometer”, Opt. Eng. 42(11) 3165–3171, November 2003.
- [26] Laurence N. Wesson, “Fiber optic photoelastic pressure sensor for high temperature gases”, SPIE, vol. 1169, pp270-279, 1986.
- [27] D. Marcuse, “Loss Analysis of Single-Mode Fiber Splices”, The Bell System Technical Journal, Vol. 56, No. 5, May-June, 1977.
- [28] <http://www.validyne.com/resp.htm>: “Estimating the Frequency Response of Variable Reluctance Pressure Sensors in Gas”.

Vita

Xingwei Wang was born in Guangzhou, P.R.China. She received her Bachelor degree in Electrical Engineering and minor in Computer Software from Zhongshan University (Sun Yat-sen University), Guangzhou, P.R. China, in September, 2000. Then she joined the Center of Optoelectronics in Zhongshan University for her graduate studies for two and a half years, focusing on the research about Erbium Doped Fiber Amplifier, and Liquid Crystal Fabry-Perot Tunable Filter. In January, 2003, she started to work at the Center for Photonics Technology at Virginia Tech for her master degree. Her research interests include optical fiber sensors for medical, chemical and industrial applications; optical imaging; MEMS technology and electromagnetic wave propagation.